UNIVERSITA' DEGLI STUDI DELLA TUSCIA

Dipartimento di Scienze Agrarie e Forestali

Corso di Dottorato di Ricerca in
Engineering for Energy and Environment
XXXV ciclo

Tesi di Dottorato

Analysis of Human Aortas through Computational Fluid Dynamics and Fluid-Structure Interaction

S.s.d. Ing-Ind/08

Tesi di dottorato di:
Dott. Simona Moretti

Coordinatore del corso
Prof. Andrea Luigi Facci

Tutore
Prof. /Dott. Danilo Monarca

Co-tutori
Prof./Dott. Andrea Luigi Facci

Prof./Dott. Flavia Tauro

A.A. 2022/23

A Daniele.

Contents

Abstract

Abnormal hemodynamics in the human aorta can lead to serious cardiovascular disease until death. While in-vivo measurements are invasive and relatively inaccurate, mathematical and computational models can provide a valuable tool for investigating the kinematics and dynamics of blood flow, and the structural response of blood vessels in cardiovascular diseases. The computational approach together with refined patient-specific geometric aortas models can be useful to acquire information about the outcome of the disease and to guide possible surgical treatment. Specifically, this thesis focuses on two different computational approaches: (i) computational fluid dynamics, and (ii) fluid-structure interaction that combines computational fluid dynamics with structural deformation analysis.

Computational fluid dynamics was applied for the in-depth study of aortic dissection in Chapter 1. Among cardiovascular diseases, aortic dissection can significantly modify hemodynamics and cause many complications because it generates an alternative path for blood flow. Thus, in Chapter 1 a healthy aorta model and three aorta dissection models were reconstructed and the flow patterns in false lumens were compared, aiming to identifying the most unfavorable condition among aortic dissection types. The results suggest that our work can be used like a guideline for future analysis of aortic dissection with computational fluid dynamics and that thrombosed false lumen has a higher probability of degeneration.

Although computational fluid dynamics is a widely validated and reliable tool, it usually does not account for wall deformation and wall mechanical properties. Fluid structure interaction is the most comprehensive approach because it allows the wall regions with a higher stress risk to be mapped, taking into account the mechanical characteristics of the wall. Among the available options, here a strongly-coupled partitioned FSI method is proposed. In the field of hemodynamics the density of the solid

and the fluid are comparable. Therefore, it is necessary to use a scheme for the coupling of the fluid-solid models that considers the inertia of the wall and limits the pressure exerted. Chapter 2 validates a fluid-structure interaction simulation of an idealized model of healthy aorta with an ad hoc scheme for coupling the fluid and solid models. The analysis shows a good agreement with the in-vivo measurements.

Introduction

Cardiovascular diseases (CVDs) are a group of disorders of heart and blood vessels that represent the leading cause of death globally [1]. In 2017, CVDs caused 17.3 million fatalities (+21.1% from 2007), and recent studies estimate that such a figure could exceed 23.6 million by 2030 [2–4]. Among CVDs, aortic dissection is the detachment of the inner from the intermediate layer of the aortic wall following the creation of one or more intimal tear [5]. This generates an alternative path for blood flow called false lumen (FL) [6, 7]. The main risk factors that prompt aortic dissection are hypertension, atherosclerosis, old age, hereditary diseases, and previous interventions such as recurrence and repair of an aneurysm [8–10].

Being aorta the largest artery in the body, its dissection can cause complications such as myocardial infarction, aortic rupture, and ischemia of the organs due to poor hemodynamics (e.g. branches connected to a badly perfused FL) [8, 11–16]. Worldwide, this life-threatening condition has a mortality incidence of $5 - 30$ cases per million, while the incidence in the emergency room is 3 [17]. Individuals aged between 65 and 75 tend to be more prone to aortic dissection, with an incidence of 35 cases per $100,000$ [15]. Further, the incidence of aortic dissection is three times higher in men than in women; however, for women the outcome is worse due to later diagnosis [18].

In high-income regions, the occurrence of aortic dissection is variable. For instance, the incidence is 3 cases per $100,000$ in the United States and Urban China [19, 20], 16 cases per $100,000$ in Sweden [21], and 17.7 cases per $100,000$ in Japan [22]. Advanced health systems and policies in these areas are largely responsible for mitigating the burden related to complications of aortic dissection [23]. However, in developing nations and medically under-served communities, aortic dissection mortality is particularly high. For instance, in developing countries the mortality rate

is 72% within one hour after diagnosis and 92% within one week [24], and among uninsured US patients, 60% of cases are detected during the autopsy and 40% suddenly die after diagnosis [25, 26]. This evidence emphasizes the relevance of early detection, adequate follow up in the chronic phase, and timely interventions to mitigate eventual complications and fatalities.

The aorta is identified by three major divisions (ascending, descending, and abdominal), as well as the aortic arch. Several classifications of aortic dissection exist based on the extension of the disease. According to the Stanford system [27], type A dissection involves the ascending aorta while type B dissection occurs in the descending division. De Bakey et al. [28], instead, identify 3 categories: (i) in type 1, the dissection affects the whole aorta, (ii) in type 2, it involves only the ascending division, (iii) and in type 3, it is localized only in the descending aorta. Following [29], aortic dissections can also be classified according to the location of the primary entry tear. Patients with aortic dissection may exhibit either fully perfused or thrombosed (completely or partially) FLs.

Dissections involve blood flow generating stresses on the aorta walls, whereby flow patterns with higher stress levels elicit pathological processes that weaken the aorta wall and, thus, promote its aneurysmatic dilation [8, 15]. High Wall Shear Stress (WSS) and its cyclic variations are key factors in dissection formation and outcome since they activate inflammatory stimuli in the inner layer endothelial cells [30, 31]. In fact, high WSS values are detected close to the tear [32–34] and dissection breakdown in association with high pressure levels [35, 36]. In addition to WSS and pressure, the Oscillatory Shear Index (OSI) is a valid predictor of WSS oscillation [37, 38]. However, it does not take into account WSS intensity, which is instead synthesized through Time-Averaged WSS (TAWSS) [39].

While in-vivo flow measurements are invasive and relatively inaccurate, Computational Fluid Dynamics (CFD) allows a thorough analysis of flow patterns, kinematics, and hemodynamic forces with high spatio-temporal resolution [40]. Such analyses enlighten the physiological processes related to the disease onset and outcome, and are a valuable decision-making guide for therapists [40–42]. Vascular surgery may also leverage on CFD to reduce surgical trauma and blood loss [43]. While idealized geometrical models are used for general studies on aorta hemodynamics [44], refined patient-specific geometrical models are required as CFD inputs to aid in the clinical assessment of aortic hemodynamics and support dissection

diagnosis [45, 46].

Comparison of numerical results to in-vivo flow measurements supports the validity of combining CFD with imaging technologies [47–51]. Specifically, image-based CFD allows to study different pathological conditions, thus identifying eventually typical flow patterns [32, 52, 53] that allow to define the emergence and outcome of the disease [34, 54, 55].

Although the benefits of CFD have already been demonstrated in therapeutic decision making for the treatment of vascular pathologies before and after operation, no clear indication is available in the literature on the likelihood of dissection degeneration in the chronic phase. In this respect, comparative CFD investigations on the hemodynamics of dissected aortas may be beneficial to inform on the disease outcome and guide eventual surgical treatment.

The aortic wall is not rigid and the contraction and dilatation of the wall are usually neglected in CFD simulation [56]. The researches compare deformable and rigid wall models and show in the deformable wall model the formation of complex flow structures with different WSS patterns, specially regarding the WSS oscillatory component [57]. A fluid−structure interaction (FSI) approach allows to obtain more accurate solution because is able to capture the wall deformation [58] and to find the mechanical alteration of the wall [59, 60], specially for the risk of rupture. Therefore, the targe to of FSI is to calculate the displacement and deformation of the wall. The criterion of maximum diameter has been widely used to study the risk of rupture in the aorta, but it has been shown that it could underestimate or overestimate the event, especially in aneurysms [61]. The literature results demonstrate that the wall rupture is formed when the strains suffered exceed its elastic limits [62]. Biomechanical tests performed on healthy and diseased aortas show wide failure stress ranges from 550kPa to 5000kPa [61].

The FSI problem can be solved with a Dirichlet-Neumann (DN) scheme for partitioned approach, which allows to treat the fluid problem separately from the structural one [63]. In case hemodynamic study, DN scheme produce numerical instabilities because the density of blood is of the same order of magnitude of the density of arterial walls [63]. The inertia of the structure can be considered by introducing Robin-Neumann (RN) scheme. According to RN scheme, the fluid problem is solved with a Dirichlet boundary condition (BC) for velocity, Robin BC for pressure at the FSI interface side-fluid [64], while the solid problem is solved with

a Neumann BC at the interface [64, 65].

Following this background, Chapter 1 shows a comparative analysis of patient-specific aortic dissections through CFD with the aim of identifying the most critical conditions and report a guidelines for future analysis of aortic dissection with CFD method. Chapter 2 describes the validation of fluid-structure interaction simulation of an idealized healthy aorta model using Robin-Neumann partitioned approach.

Chapter 1

Analysis of Patient-Specific Aortic Dissections through CFD

Aortic dissection is a life-threatening vascular disease associated with high rates of morbidity and mortality, especially in medically underserved communities. Understanding patients' blood flow patterns is pivotal for informing evidence-based treatment as they greatly influence the disease outcome. The present study investigates the flow patterns in the false lumen of three aorta dissections (fully perfused, partially thrombosed, and fully thrombosed) in the chronic phase, and compares them to a healthy aorta. Three-dimensional geometries of aortic true and false lumens (TLs and FLs) are reconstructed through an ad hoc developed and minimally supervised image analysis procedure. Computational fluid dynamics (CFD) is performed through a finite volume unsteady Reynolds-averaged Navier–Stokes approach assuming rigid wall aortas, Newtonian and homogeneous fluid, and incompressible flow. In addition to flow kinematics, we focus on time-averaged wall shear stress and oscillatory shear index that are recognized risk factors for aneurysmal degeneration. Our analysis shows that partially thrombosed dissection is the most prone to false lumen degeneration. In all dissections, the arteries connected to the false lumen are generally poorly perfused. Further, both true and false lumens present higher turbulence levels than the healthy aorta, and critical stagnation points. Mesh sensitivity and a thorough comparison against literature data together support the reliability of the CFD methodology. Image-based CFD

simulations are efficient tools to assess the possibility of aortic dissection to lead to aneurysmal degeneration, and provide new knowledge on the hemodynamic characteristics of dissected versus healthy aortas. Similar analyses should be routinely included in patient-specific hemodynamics investigations, to plan and design tailored therapeutic strategies, and to timely assess their effectiveness.

The chapter is organized as follows. In section 1.1 the four dissected aortas models are presented and the physical model is described. The methods are accurately describe in section 1.2. Specifically, the procedure for reconstructing the aortic geometry models is reported in 1.2.1 and the numerical modeling methodology is described in section 1.2.2. In section 1.3 the models grid sensitivity and validation are shown. The comparison between the simulation results are shown in section 1.4. Specifically, the flow distribution are in subsection 1.4.1, the flow kinematic in subsection 1.4.2, and the hemodynamic forces are in subsection 1.4.3. Section 1.5 summarizes the main findings from the present Chapter.

1.1 Problem Statement

The aim of this Section is to present the dissected aortas, and describe the hypotheses and the equations governing the physics of the system. We reconstruct four patient-specific aortic models from in vivo measures: (i) a benchmark model for a healthy patient (healthy aorta, HA, Figure 1.1a); (ii) a model for a patient who exhibited fully perfused FL (fully perfused type B/3 aorta, FPA, Figure 1.1b); (iii) a model for a patient with a partially thrombosed FL (partially thrombosed type A/1 aorta, PTA, Figure 1.1c); and (iv) a model for a patient who developed complete FL thrombosis following thoracic endovascular aortic repair (fully thrombosed B/3 type aorta, FTA, Figure 1.1d). The FPA model geometry presents an FL that originates from a single tear just downstream from the aortic arch and continues down to the iliac arteries without any further connections to the true lumen (TL, in gray in Figure 1.1b). The FL diameter tends to be larger than the TL, especially from the aortic arch down to the abdominal branches. The PTA geometry has a FL that originates in the ascending aorta and then merges back into the abdominal TL. At the beginning of the descending aorta, the FL is thrombosed, not displayed in Figure 1.1c. The considerably dilated aortic arch FL (in green in Figure 1.1c) is fed blood from one tear up and one downstream the arch, while the

abdominal TL feeds blood to the FL (in gray in Figure 1.1c) through five additional tears. The FL merges back into the TL three diameters above the iliac branches. Each perfused FL reach causes an abrupt reduction of the TL cross-section at the aortic arch and in proximity of the onset of the abdominal FL, respectively. Patient FTA was treated with two consistent overlapping Valiant devices (Valiant Captivia, Medtronic Vascular, Santa Rosa, California; proximal diameter: 40 mm, distal diameter: 40 mm, endoprosthesis length: 200 mm) to induce FL thrombosis from the aortic arch down to the left renal artery. Figure 1.1d only depicts the perfused abdominal FL in gray. The TL feeds blood to the abdominal FL through two tears just below the left renal artery. The FTA geometry presents the largest inlet section among all models, and a significant restriction at the onset of the perfused FL. In all geometries, the left renal artery originates from the abdominal FL, which was purposely left perfused in the FTA.

For this study, formal ethical approval was not required, as prior agreement was established to undertake computational modeling work using totally anonymized images without requiring further specific ethics committee agreement for individual patients. All data were analysed anonymously and patient information was deidentified prior to analysis.

We assume the aorta rigid and large enough to consider the blood as a Newtonian and homogeneous fluid [32], while the flow can be safely considered incompressible [66]. Such a flow is modeled by the following Navier–Stokes (N-S) equations (Equation (1.1)) and mass conservation equation (Equation (1.2)):

$$\rho\frac{\partial\vec{u}}{\partial t} + \rho(\vec{u}\cdot\nabla)\vec{u} = -\nabla p + \mu\nabla^2\vec{u}\,, \tag{1.1}$$

$$\nabla\cdot\vec{u} = 0\,, \tag{1.2}$$

where t is the time, $\vec{u} = (u_x, u_y, u_z)$ is the velocity field, p is pressure, $\mu = 3.71\times10^{-3}\,\mathrm{kg/m\,s}$ is the dynamic viscosity [67], and $\rho = 1060\,\mathrm{kg/m^3}$ the blood density [48].

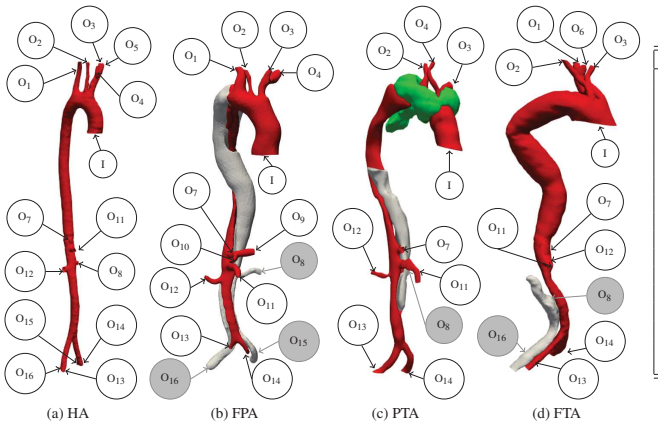

(e)

ID	Artery name
I	Inlet
O_1	Left subclavian
O_2	Left common carotid
O_3	Right common carotid
O_4	Right subclavian
O_5	Right internal common carotid
O_6	Anonymus
O_7	Celiac
O_8	Left renal
O_9	Splenic
O_{10}	Epatic
O_{11}	Superior mesenteric
O_{12}	Right renal
O_{13}	Right common iliac
O_{14}	Left common iliac
O_{15}	Left internal common iliac
O_{16}	Right internal common iliac

Figure 1.1: *Representation of the four considered aorta models with relative arteries. TL is in red, FL is in gray and green: (**a**) HA; (**b**) FPA; (**c**) PTA where the aortic FL is in green and the abdominal FL in gray; (**d**) FTA; (**e**) names of the branches. The branches connected to the FL are highlighted in gray.*

We select the orthogonal Cartesian reference frame $O - xyz$ with the z-axis directed upward according to the direction of the flow leaving the heart through the ascending aorta, the y-axis according to the anterior–posterior direction, and the origin O located as schematized in Figure 1.2.

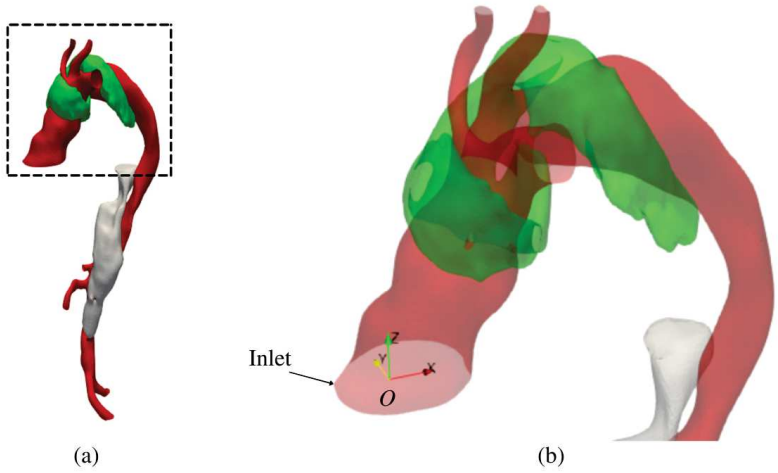

Figure 1.2: *Representative 3D domain for PTA including the TL (red) and the FL (green and gray). (**a**) Complete geometry and (**b**) focus on the reference system whose origin O is in the centroid of the inlet section.*

The Reynolds number, $\mathrm{Re} = u_\mathrm{I}\rho D/\mu$ [67], estimated as a function of the inlet section diameter D and of the average inlet velocity u_I, defines the flow regime. The blood flow is pulsating [56] and $150 < \mathrm{Re} < 6000$ [67]. With such figures, the flow varies among laminar, transitional, and turbulent regimes as a function of t during the cardiac cycle.

We focus on pressure and shear forces that the blood flow generates on the aorta wall as well as on coherent flow structures. Specifically, $\overrightarrow{\mathrm{WSS}}$ is determined through Equation (1.3) after solving Equations (1.1) and (1.2):

$$\overrightarrow{\mathrm{WSS}} = -\mu \frac{\partial \vec{u}}{\partial \hat{n}}\bigg|_{\mathrm{wall}} , \tag{1.3}$$

where $\hat{n}$ is the unit vector normal to the wall [68]. We will refer to the magnitude of $\overrightarrow{\mathrm{WSS}}$ as WSS. The Wall Shear Force (WSF) is defined as:

$$\overrightarrow{\mathrm{WSF}} = \int_s \overrightarrow{\mathrm{WSS}}\, \mathrm{d}s\,, \tag{1.4}$$

where $\mathrm{d}s$ is the surface element.

We identify the vortex structures through the 2nd invariant of the velocity gradient tensor:

$$Q = \frac{1}{2}\left(||\underline{\Omega}||^2 + ||\underline{S}||^2\right) , \tag{1.5}$$

where $\underline{S}$ is the stress rate tensor and $\underline{\Omega}$ is the vorticity tensor. The Q-criterion defines the vortexes as connected fluid regions with a positive Q [69]. Finally, turbulence intensity [70]

$$T = \frac{\sqrt{\frac{2}{3}k}}{u}, \tag{1.6}$$

describes the level of flow turbulence, being u the magnitude of the instantaneous local velocity, and k the turbulent kinetic energy.

1.2 Methods

1.2.1 Three-Dimensional Geometry Reconstruction from CT and Models for CFD Simulation

Cephalocaudal thoracic and abdominal CT scans were executed from 2013 to 2020. Table 1.1 details the CT scan settings, where the field of view was consistently set to 512 $\times$ 512 pixels, the gantry detector tilt to 0°, and the tube voltage (KPV) to 120 kV.

Table 1.1: *CT scan settings for all patients.*

	HA	**FPA**	**PTA**	**FTA**
Age (years)	26	48	65	70
Gender	M	M	M	F
Bit depth	12	12	16	16
In-plane resolution (mm)	0.9766	0.7910	0.8125	0.8086
Slice thickness (mm)	1.5	1.0	2.5	1.25
Tube current (mA)	150	510	404	350

The patient-specific aortic geometric models are reconstructed from CT scan DICOM images [71] through an ad hoc procedure developed in the Matlab environment (Figure 1.3). The steps of the procedure are the following: (i) manual identification of a region of interest enclosing both true and false lumens; (ii) contrast enhancement through histogram equalization; (iii) image binarization by thresholding; and (iv) object boundary identification through the Moore Neighbor tracing algorithm modified by Jacob's stopping criteria [72]. In case of poor visibility of the aortic dissection, image contrast is enhanced through adaptive thresholding. Namely,

a threshold mask image is introduced based on a local 4-connected pixel neighborhood. Then, the mean for the local neighborhood is compared to a constant threshold: if the mean is higher than such a value, a constant value is subtracted from the central pixel of the mask. This technique affords a reduction of the background noise through smoothing of the lumen boundaries.

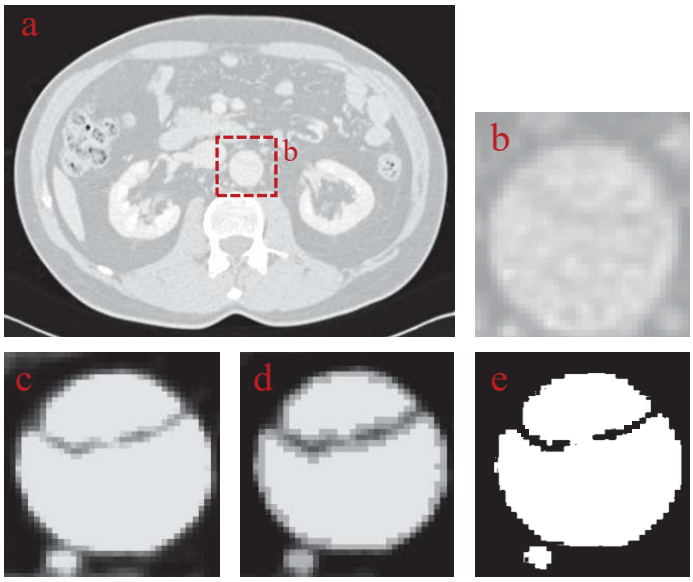

Figure 1.3: *Image-based procedure for reconstructing the aortic geometric models: (**a**) example of DICOM image from the FPA CT scan sequence; (**b**) identification of the region of interest; (**c**) enhancement of image contrast; (**d**) smoothing of lumen boundaries through the ad hoc developed image filter; and (**e**) image binarization.*

Such a procedure returns a point cloud for each geometry (Figure 1.4a) that is processed through Rhinoceros v.7 to obtain mathematical models of the aorta. First, the points are interpolated through a polygonal mesh [73] (Figure 1.4b). Then, the Mesh2Surface Rhinoceros extension creates a structured quadrilateral surface mesh (Figure 1.4c) through the quadrilateral surface mesh SubD modeling technique [74]. After manual revision and cleaning of the surface features, the geometry is saved in the Initial Graphics Exchange Specification (IGES) file format [75] (Figure 1.4d).

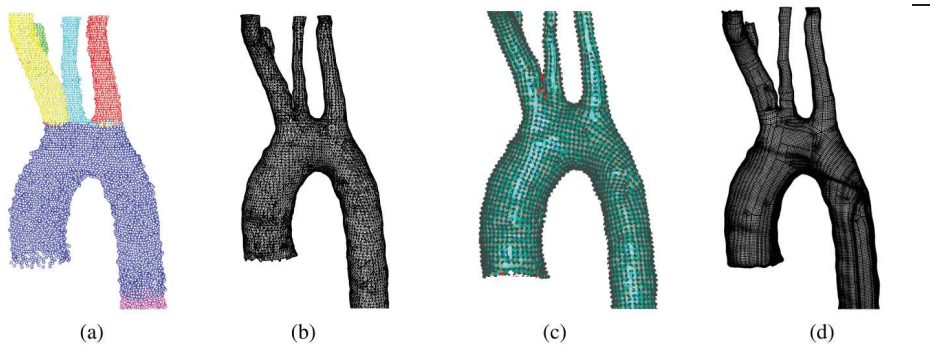

Figure 1.4: *Representation of the procedure for geometry definition from point clouds to mathematical surface description. (**a**) Point cloud example; (**b**) 3D polygonal mesh resulting from points interpolation; (**c**) quadrilateral mesh obtained from Mesh2Surface with critical spots evidenced by red points; (**d**) final geometry representation.*

1.2.2 Numerical Modelling of Blood Flow

We use the RANS [76–78] approach to numerically solve Equations (1.1) and (1.2) in their Reynolds-Averaged form. We assume the Launder and Sharma $k-\varepsilon$ turbulence model [79] to close the Reynolds Stresses term. In fact, this model is suitable to solve the low Reynolds number phenomena [79, 80] (e.g., where the non-dimensional wall distance in wall units is small, $y^+ < 5$ [78]) relevant in the aortic blood flow, which is in the transitional regime [76]. Specifically, it does not use any wall functions to solve the boundary layer [80], allowing a reliable evaluation of the WSS [81]. Such a closure model introduce three variables (k; the turbulent kinetic energy dissipation rate, ϵ; and the turbulent viscosity, ν_t) and the relative transport equations.

Differential equations are discretized though a finite volume approach with collocated variable arrangement [82] implemented in the software package OpenFOAM-v7 [83].

The Pressure-Implicit with Splitting of Operators (PISO) algorithm [84] solves the pressure–velocity coupling and the non-linearity in Equations (1.1) and (1.2). The Euler implicit scheme [85] is selected for temporal integration. The Gauss linear scheme is used for the spatial interpolation of the gradients. The convective terms of Equations (1.1) and (1.2) are interpolated with the second-order Gauss GammaV scheme [82] with weight coefficient $\phi = 0.25$. The convective terms for the k and ϵ

equations of the Launder and Sharma model are interpolated though the Linear Upwind scheme.

The Geometric-Algebraic Multi-Grid (GAMG) iterative algorithm is used to solve the linear system of equations obtained from temporal and spatial discretization of the pressure equation, while the iterative symmetric Gauss–Seidel method solves the linear systems of equations for u, k, and ϵ [70]. The time-step length is 0.001 and the time-stepping strategy is Co-dependent. The maximum value of Courant number is 0.5 Tolerances are reported in Table 1.2.

Table 1.2: *Tolerance values for iterative linear system solvers.*

Variable	Tolerance	Relative Tolerance
p/ρ	$10^{-6}\,\mathrm{m}^2/\mathrm{s}^2$	0.01
u	$10^{-6}\,\mathrm{m}/\mathrm{s}$	0.05
k	$10^{-6}\,\mathrm{m}^2/\mathrm{s}^2$	0.05
ϵ	$10^{-6}\,\mathrm{m}^2/\mathrm{s}^3$	0.05
ν_t	$10^{-6}\,\mathrm{m}^2/\mathrm{s}$	0.05

Table 1.3 summarizes the mathematical formulation for all the boundary conditions (BCs). In particular, a velocity inlet type BC approximates the flow that leaves the heart entering the computational domain through surface I (see the inlet identifiers in Figure 1.1). Specifically, $u_0(t)$ in Equation 1.9 is reported in Figure 1.5a. Therein, points are sampled from [48], where $u_0(t)$ was obtained through in vivo PC-MRI of the ascending aorta root. We use a Fast Fourier Transform (FFT)[86] to interpolate such discrete measures to the continuous periodic function also depicted in Figure 1.5a. The correlation coefficient is $R^2 = 0.999$ assuming 8 modes and the parameters reported in Figure 1.5b. We note that the peak systolic velocity is about $0.5\,\mathrm{m}/\mathrm{s}$ and the average inlet flow is about $6\,\mathrm{l}/\mathrm{min}$ [87]. The duration of a cardiac cycle is $\mathcal{T} = 0.96\,\mathrm{s}$. The maximum Reynolds number is 4600. Note that to capture the flow kinematics during diastole, $u_0(t)$ allows backflow through I ($u_0(t) < 0$ in Figure 1.5), see also [88].

We use inlet-outlet type BCs for all the other permeable boundaries identified by $[\mathrm{O}_1 \ldots \mathrm{O}_{13}]$ in Figure 1.1. Such BC automatically switches between inlet and outlet modeling as a function of the flow direction [89], see Equations (1.9) in Table 1.3. Therein, $p_{\mathrm{O}_i}(t)$ is determined through the 3-element Windkessel model (Equation (1.7), [90]) that simulates the

Table 1.3: *Mathematical description of the assumed boundary conditions where $\hat{n}$ is the unit normal to the model surface.*

Boundary	Boundary Model Equation				
I	$\vec{u} = u_0(t)\hat{n}$	$\frac{\partial p}{\partial \hat{n}} = 0$	$k = k(t_0)$	$\epsilon = \epsilon(t_0)$	(1.8)
$[O_1 ... O_{13}]$	$\begin{cases} \frac{\partial \vec{u}}{\partial \hat{n}} = 0 \\ \vec{u} = u_{O_i} \end{cases}$	$\begin{cases} p_{O_i}(t) \\ \frac{\partial p_{O_i}(t)}{\partial \hat{n}} = 0 \end{cases}$	$\begin{cases} \frac{\partial k}{\partial \hat{n}} = 0 \\ k = k_{O_i} \end{cases}$	$\begin{cases} \frac{\partial \epsilon}{\partial \hat{n}} = 0 & \text{outflow} \\ \epsilon = \epsilon_{O_i} & \text{inflow} \end{cases}$	(1.9)
Wall	$\vec{u} = 0$	$\frac{\partial p}{\partial \hat{n}} = 0$	$k = 10^{-10}$	$\epsilon = 10^{-10}$	(1.10)

resistance of the remaining vascular peripheral network [49, 91]

$$\frac{Q_{\mathrm{O}_i}(t)}{C} = \frac{\mathrm{d}(p_{\mathrm{O}_i}(t) - R_1 Q_{\mathrm{O}_i}(t))}{\mathrm{d}t} + \frac{1}{R_2 C}(p_{\mathrm{O}_i}(t) - R_1 Q_{\mathrm{O}_i}(t)) \ . \qquad (1.7)$$

In Equation (1.7) Q_{O_i} is the volume flow rate at the outlet O_i, C is the network compliance, R_1 is the proximal resistance, and R_2 is the distal resistance. We estimate the constants C, R_1, and R_2 following the procedure in [91] and reported in Appendix A. Equation (1.7) is integrated in time through the Euler explicit method.

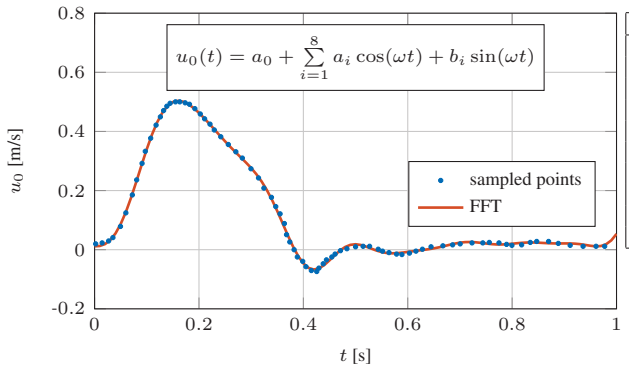

(a)

$\omega = 6.541$ rad/s		
mode	a	b
0	0.115 m/s	–
1	0.069 m/s	0.177 m/s
2	-0.112 m/s	0.072 m/s
3	-0.048 m/s	-0.031 m/s
4	-0.013 m/s	-0.004 m/s
5	-0.017 m/s	-0.030 m/s
6	0.014 m/s	-0.005 m/s
7	-0.003 m/s	-0.002 m/s
8	0.006 m/s	-0.003 m/s

(b)

Figure 1.5: *Representation of u_0 as a function of t: (**a**) sampled values from [48] and FFT; (**b**) coefficients of the FFT transform.*

The aortic walls are rigid and we select the no-slip BC without wall functions, as reported by Equation (1.10) in Table 1.3.

The arteries are elongated with virtual cylinders to avoid the excessive proximity of the BCs to flow regions with significant gradients to cause numerical instability. The length of such cylinders is about 10 times the branch diameter.

We initialize the domain assuming $p(t=0)=0$ and $\vec{u}(t=0)=\vec{0}$. We then estimate the turbulent flow variables as:

$$k(t_0) = \frac{1}{2}\max\left[(u_0(t))^2\right] , \tag{1.8a}$$

$$\epsilon(t_0) = \frac{C_\mu^{0.75} k^{1.5}}{L} , \tag{1.8b}$$

$$\nu_t(t_0) = \rho C_\mu \frac{k^2}{\epsilon} . \tag{1.8c}$$

where $L = 0.038D$ is the reference length scale [85], and $C_\mu = 0.09$ [79].

We use an unstructured meshing approach for surface and volume through the ANSA v.21.1.2 software. First, we create a triangular surface mesh using the CFD algorithm (Figure 1.6b), which determines the node distribution according to the curvature of the surface [92]. Specifically, we assume an interior growth rate of 1.1 and a distortion angle of 20. Then, we create 5 layers, assuming a linear growth factor of 1.2. The remaining volume is discretized using tetrahedra through the tetra-CFD algorithm with maximum growth factor of 1.1 (Figure 1.6c). Finally, the grid is converted into a polyhedral mesh (Figure 1.6d) to reduce the number of elements, improve solution convergence, and, ultimately, speed up execution [93].

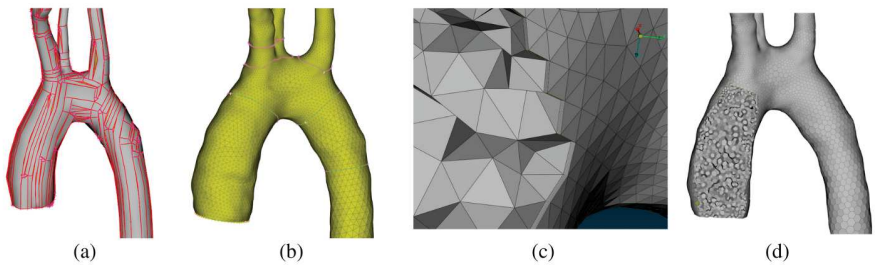

Figure 1.6: *Representation of the procedure to obtain the computational mesh from the CAD model. (**a**) CAD model (i.e., mathematical surface description); (**b**) triangular surface mesh; (**c**) tetrahedral volume mesh with focus on the surface layers; (**d**) polyhedral volume mesh.*

Numerical simulations are performed using parallel computing through the public domain openMPI implementation of the standard message passing interface (MPI) [83]. We used the Scotch decomposition method for domain partitioning (20 sub-domains). Parallel computing was performed on 20 Intel® Xeon® E5-2680-v2-@-2.80 GHz processors and took between 24 h and 120 h as a function of the geometry. Equivalently, the velocity update was between 631,000 nodes per second and 850,000 nodes per second.

1.3 Convergence, Mesh Sensitivity, and Validation

1.3.1 Convergence

The assumed initial conditions significantly impact the simulation for the first cardiac cycles. We evaluate such an influence through the following mean error of the instantaneous average pressure on the surface I, $\mathcal{P}_{\mathrm{I}}(t)$:

$$\Delta_{\mathcal{T}} = \frac{1}{N_s} \sum_{l=1}^{N_s} \frac{\mathcal{P}_{\mathrm{I}}(t(l)) - \mathcal{P}_{\mathrm{I}}(t(l) - \mathcal{T})}{\mathcal{P}_{\mathrm{I}}(t(l))} \,. \tag{1.9}$$

In Equation 1.9 N_s is the number of samples per cycle. We perform the convergence study on the HA, whereby $\Delta_{\mathcal{T}} < 5\%$ for the 4th cycle. Thereof, we simulate the flow through all the aorta models for 4 cycles and, in the following, we present results for the 4th cycle.

1.3.2 Mesh Sensitivity

We also assess the impact of the mesh quality by comparing simulation results for 6 different HA domain discretizations (Table 1.4). This aims at demonstrating the independence of results from the grid.

Table 1.4: *Mesh sensitivity analysis.* ***(a)*** *Relevant mesh properties: number of polyhedra and maximum value of the spatially averaged y^+;* ***(b)*** *evaluation of Δ_{WSF} in percentage for all the mesh combinations. Warm colors indicate higher errors.*

Mesh	n° Polyhedra	y^+
A	310,000	1.7
B	411,000	0.93
C	600,000	0.94
D	220,000	0.56
E	706,000	0.27
F	286,000	0.24

(a)

Mesh	A	B	C	D	E	F
A	-	24	28	12	15	16
B	24	-	10	24	23	26
C	28	10	-	28	26	29
D	12	24	28	-	14	10
E	15	23	26	14	-	11
F	16	26	29	10	11	-

(b)

We first analyze the mesh effects on the inlet and outlet pressures. Specifically, we compare $\mathcal{P}_{\mathrm{I}}$ and the average pressure $\mathcal{P}$ on O_{13} ($\mathcal{P}_{\mathrm{O}_{13}}$) for meshes A and B. For instance, for $\mathcal{P}_{\mathrm{I}}$, the cycle average pressure difference is computed as $\Delta_{p,\mathrm{I}} = \frac{1}{N_s}\sum_{l=1}^{N_s} \frac{|\mathcal{P}_{\mathrm{I}}^A(t(l)) - \mathcal{P}_{\mathrm{I}}^B(t(l))|}{\mathcal{P}_{\mathrm{I}}^A(t(l))}$. Both $\Delta_{p,\mathrm{I}}$ and $\Delta_{p,\mathrm{O}_{13}}$ are below or equal to 0.1%.

Finally, we assess the sensitivity of WSF on the grid as in [94] through Equation 1.10.

$$\Delta_{\mathrm{WSF}} = \frac{1}{N_s}\sum_{l=1}^{N_s} \frac{|\mathrm{WSF}_j(t(l)) - \mathrm{WSF}_m(t(l))|}{\max\left[\mathrm{WSF}(t(l))\right] - \min\left[\mathrm{WSF}(t(l))\right]}\,, \tag{1.10}$$

where j and m identify the different grids, and WSF is the magnitude of $\overrightarrow{\mathrm{WSF}}$. Warm colors in Table 1.4b indicate higher Δ_{WSF}. Entries in the bottom-right quadrant all exhibit cold colors, thus showing that the y^+ dominates the mesh sensitivity compared to the grid density [95]. In fact, the error is low for mesh combinations with similar y^+ and a diverse number of polyhedra (see, for example, E–F and B–C). Conversely, large Δ_{WSF} are attained for mesh combinations with comparable numbers of polyhedra and different y^+ values (see, for example, C–E). Since low y^+ values yield low Δ_{WSF}, and a low number of polyhedra results in a smaller computational burden, we adopt mesh F as a template for all geometries.

In Table 1.5, we report the mesh quality evaluated through its non-orthogonality, skewness, and aspect ratio, as defined in [70]. In agreement with standard procedures in CFD for optimal solution convergence and high solution quality, the non-orthogonality is lower than 65 and the skewness is lower than 4, respectively, for all models.

Table 1.5: *Relevant quality parameters for the considered meshes.*

	HA	**FPA**	**PTA**	**FTA**
n surface elements	79,900	107,867	125,146	107,156
n polyhedra	272,000	449,424	511,223	480,490
Max non-orthogonality	64.24	64.98	64.65	64.78
Max skewness	2.36	3.90	3.90	3.53
Max aspect ratio	49.1	49.9	49.9	48.5
y^+	0.239	0.243	0.296	0.125
First-layer thickness	2%	2%	2%	2%

1.3.3 Validation

Since to the best of our knowledge in vivo measurements are not available, we compare our results for the HA against simulation data from the literature. Specifically, we estimate $\mathcal{P}_{\mathrm{I}} - \mathcal{P}_{\mathrm{O}_{13}} \simeq 1.6\,\mathrm{mmHg}$, which is in line with the values in [49], which are approximately 1 mmHg.

Table 1.6 compares the percentage of inlet flow for three groups of arteries (superior, abdominal, and iliac) for our HA simulation to results from [96]. Values for the iliac flow show a remarkable agreement, while moderate differences are detected for superior and abdominal arteries. However, such differences are in line with the difference modeling assumptions and geometries. In fact, we perform 3D simulations of real aorta models assuming rigid walls. Conversely, [96] uses a one-dimensional approach with custom BCs for 3D flow regions (e.g., junctions) and for wall elasticity, while the [97] study simplified rigid geometries.

Table 1.6: *Volume flow distribution for superior, abdominal, and iliac arteries (%).*

Arteries	**Alastruey et al. [96]**	**Xiao et al. [97]**	**Park et al. [98]**	**HA**
Superior	30%	21%	27%	38%
Abdominal	52%	58%	51%	44%
Iliac	18%	22%	22%	17%

Lantz et al. [76] estimate that the maximum WSS $\simeq 45\,\mathrm{Pa}$ and is located between subclavian and carotid roots during systolic peak. Similarly, our simulation yields WSS $\simeq 54\,\mathrm{Pa}$ in the same region as evidenced

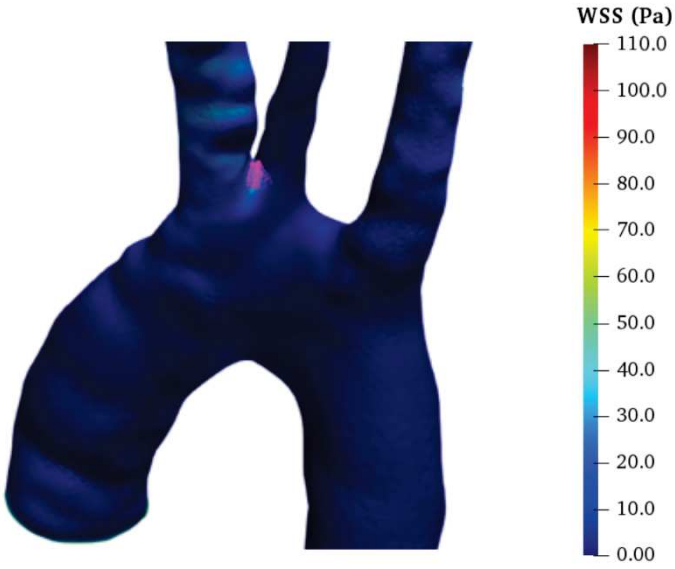

Figure 1.7: *Values of WSS in the region measured by [76]. Maximum WSS values located between the subclavian and carotid roots.*

in Figure 1.7.

For a final validation, we compare a few distinctive features of the flow patterns of HAs with references [76, 88]. Figure 1.8a shows the streamlines in the aortic arch at the systolic peak where the uniform flow is prevalent as also highlighted in [76]. Specifically, the flow divides within the branches of the aortic arch with a pattern similar to that evidenced in [76]. At diastole, the model correctly describes the retrograde and disturbed flow patterns in the descending aorta (see Figure 1.8b), as reported in [76, 88].

In agreement with [76], Figures 1.9a,b clearly depict asymmetric flow in the ascending and uniform flow in the descending aorta, respectively. As expected, flow asymmetry in the ascending aorta is due to the superior branches flow. Likewise [76], the pattern becomes more chaotic and turbulent in the deceleration phase at time 0.3 s (Figure 1.9c) and in the diastolic phase at time 0.5 s (Figure 1.9d). Finally, the section between the upper arteries exhibits the same flow pattern of [76] at all time-steps (Figures 1.9a–d).

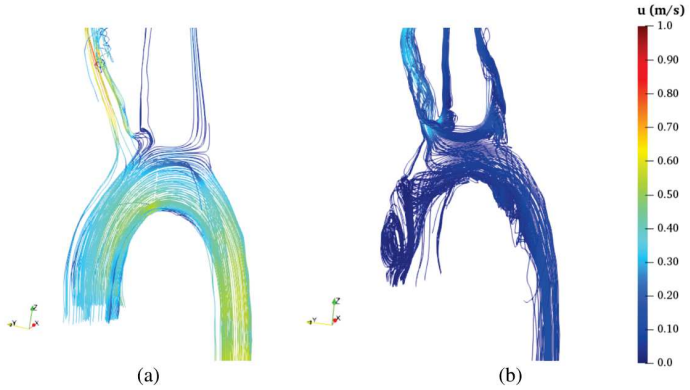

Figure 1.8: *Representation of velocity streamlines in the aortic arch for the HA: (**a**) systolic peak ($t = 0.15\,\mathrm{s}$), (**b**) diastole ($t = 0.5\,\mathrm{s}$).*

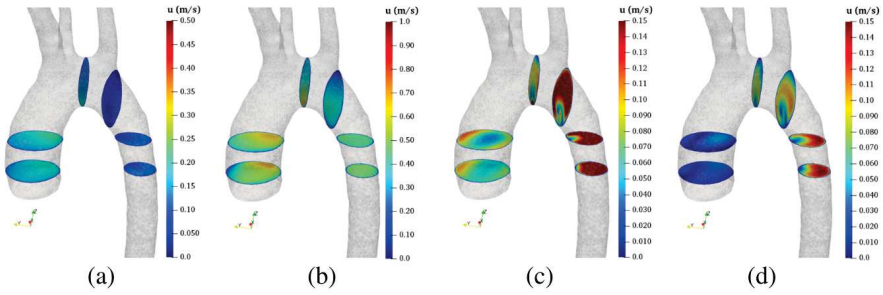

Figure 1.9: *Velocity magnitude contours for the HA: (**a**) acceleration phase ($t = 0.1\,\mathrm{s}$); (**b**) systolic peak ($t = 0.15\,\mathrm{s}$); (**c**) deceleration phase ($t = 0.3\,\mathrm{s}$) and (**d**) diastole ($t = 0.5\,\mathrm{s}$).*

Table 1.7: *Volume flow distribution for the branches (%).*

	O_1	O_2	O_3	O_4	O_5	O_6	O_7	O_8
HA	9.5	5.4	16.5	3.7	3.1	-	9.7	11.4
FPA	9.4	2.6	7.3	5.3	-	-	3.3	6.4
PTA	-	9.63	11.8	10.5	-	-	15.2	1.3
FTA	12.8	6.1	4.3	-	-	12.2	19.5	0.1
	O_9	O_{10}	O_{11}	O_{12}	O_{13}	O_{14}	O_{15}	O_{16}
HA	-	-	9.1	14	7.2	4.9	2.96	2.2
FPA	2.7	0.6	2.5	1.8	2.6	2.4	24.8	28.3
PTA	-	-	11.2	2.6	21.6	16.2	-	-
FTA	-	-	6.2	5.2	12.7	19	-	1.8

1.4 Results and Discussion

1.4.1 Flow Distribution

Each aortic dissection impacts the distribution of the blood volume flow through the different branches in a peculiar way (see Table 1.7). In the following, we quantify such impacts by computing the percentage volume flow increase/decrease for each outlet with respect to HA. In FPA, the FL drains the TL flow [48]. As a consequence, the abdominal branches (that, in this case, are connected to TL) undergo a significant flow reduction equal to 66% (O_7), 72% (O_{11}) and 88% (O_{12}). Conversely, the volume flow increases by approximately 90% in the iliac branches (O_{15}, O_{16}) that are connected to the FL. For the PTA, the flow through the aortic arch FL reduces the flux through O_3 by approximately 30%, while it increases the flux at O_2 and O_4 by 44% and 65%, respectively. Note that the left renal artery (O_8) is connected to the abdominal FL in both PTA and FTA and its flow is reduced by 89 % and 99%, respectively. Finally, for the PTA, the right renal artery flow (O_{12}) is reduced by 82%, as a consequence of the abdominal FL flow that originates from two tears in the abdominal aorta region. While these findings may be patient-specific since they depend on the number and location of the intimal tears, they are well in agreement with clinical evidence. In fact, the paravisceral segment FL thrombus (as in PTA and FTA) is a frequent cause of visceral blood flow reduction in the chronic phase of aortic dissection [99].

1.4.2 Flow Kinematics

We analyse the flow kinematics for all the models at the systolic peak ($t = 0.15\,\mathrm{s}$), where the velocity is maximum, and at diastole ($t = 0.5\,\mathrm{s}$), where retrograde flow occurs in ascending aorta and the turbulence levels are higher. Further, we study in detail the streamlines patterns in the proximity of the tears, which are relevant flow regions in terms of aortic dissection outcome [100]. Finally, we dissect u_z patterns at diastole. Enhanced-visualisation streamlines and Q contours are available at https://github.com/andrea-facci/Aorta as supplementary movies. In all diseased aortas, the velocity pattern is less homogeneous than in HA (Figures 1.10 and 1.11), and the flow accelerates along the abdominal aorta and the iliac branches (Figure 1.10) due to abrupt diameter variations in the TL. Such a result is more prominent in the FPA TL and in both PTA TL and FL, while the flow in the FL of the FPA (Figure 1.10b) and in the TL of the FTA (Figure 1.10d) is ordered and similar to the pattern of the HA (see also [76]). The highest velocity magnitude locates in the PTA TL that has the smallest cross-section, and three major restrictions identifiable in Figure 1.10c as the regions at high velocity values. One of these restrictions is located in the arch and is followed by an abrupt section enlargement that yields recirculating flow (see Figure 1.11c and the focused view in Figure 1.12b). The other two restrictions are located in the abdominal aorta. Therein, blood flow in the FL is fed from the TL exclusively through five tears located below O_8 (Figure 1.12c). As a consequence, the upper part of the abdominal FL is washed by an ascending and recirculating flow as displayed by low u closed streamlines. Similar evidence can be found in [32]. In the FTA, the tears are also located below O_8 (Figure 1.12d), which receives its flux through an ascending flow. Streamlines show a helical flow pattern of very low velocity (Figures 1.12c,d). This is consistent with reduced volume flows through O_8 (see Table 1.7).

In HA, the Q pattern is regular, with stable organized vortexes located close to the walls (Figure 1.13a) that represent the helical flow developing along the entire aorta (similar results are found in [88]). These structures are continuous, organized, and regular (see also [101]), and the flow pattern does not show stagnation zones (black arrows in Figures 1.13 and 1.14). Moreover, such vortexes are stable in time, as arguable by comparing Q values for systole (Figure 1.13a) and for diastole (Figure

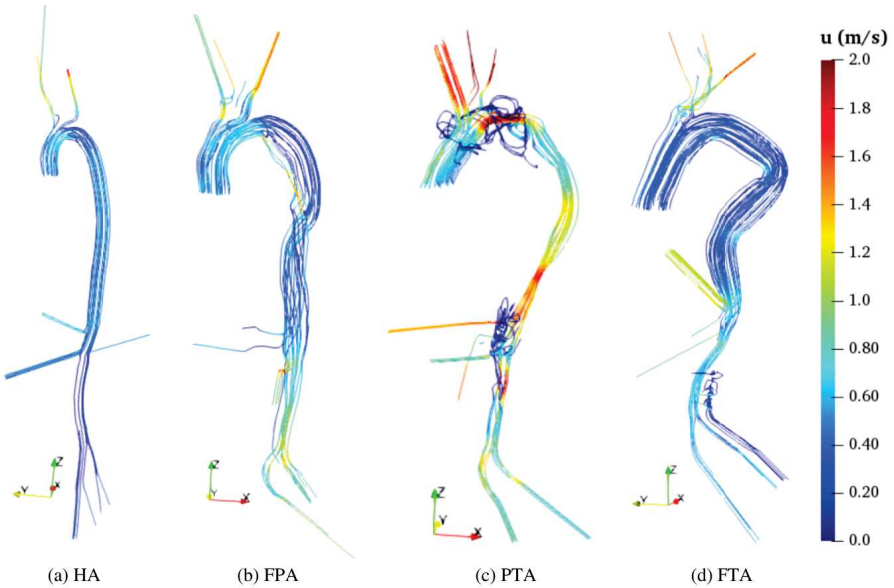

Figure 1.10: *Streamlines at* $t = 0.15\,\mathrm{s}$ *(systolic peak).*

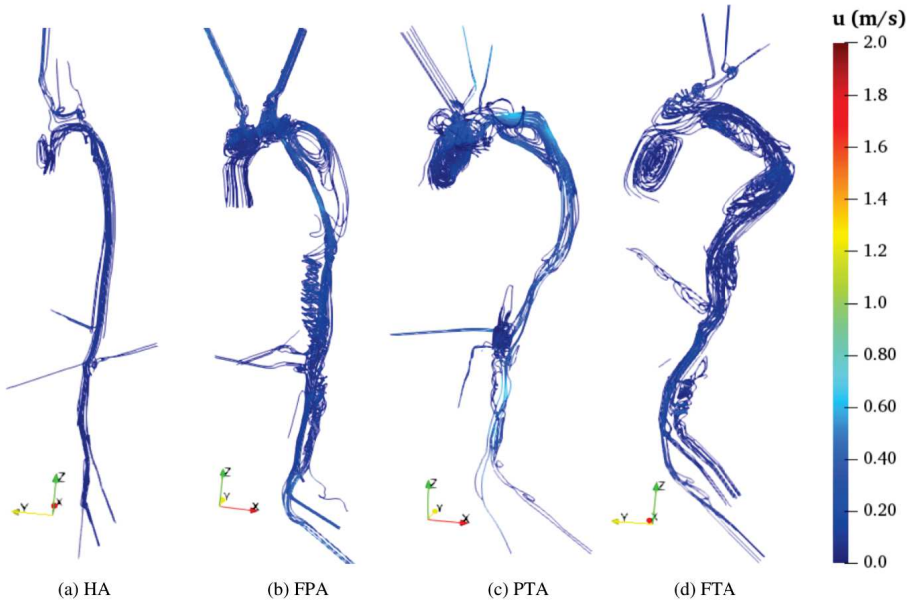

Figure 1.11: *Streamlines at* $t = 0.5\,\mathrm{s}$ *(diastole).*

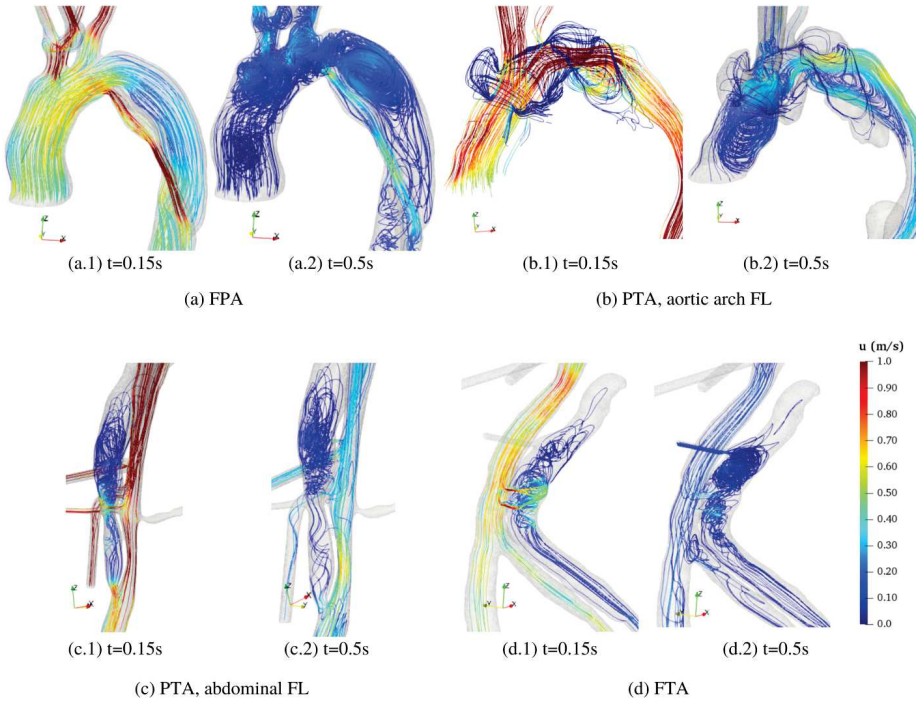

Figure 1.12: *Detail of streamlines at the tears for* $t = 0.15\,\mathrm{s}$ *(systolic peak) and* $t = 0.5\,\mathrm{s}$ *(diastole).* (**a**) *Tear in the FPA;* (**b**) *two tears in the PTA aortic arch;* (**c**) *six tears in the PTA abdominal aorta;* (**d**) *two tears in FTA.*

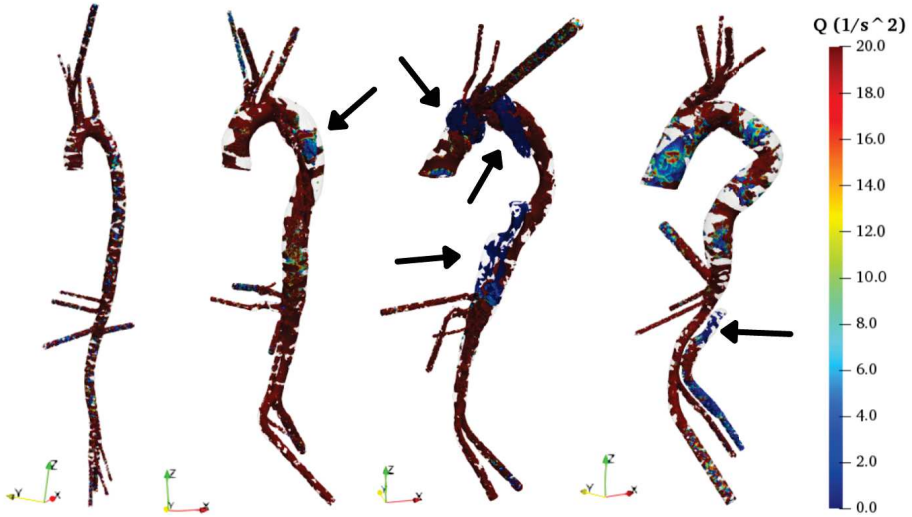

Figure 1.13: *Q contour plots at $t = 0.15\,\mathrm{s}$ (systolic peak). Gray colour represents $Q < 0$, which are not significant [102]. Black arrows identify relevant stagnation regions.*

1.14a). However, at systole, coherent structures involve the whole domain, while, at diastole, they mainly develop along the descending and abdominal aorta. In fact, at diastole, vortex structures originate within the arch and proceed through the descending aorta [101].

In dissected aortas, coherent structures are fragmented (in particular in FPA and PTA), and stagnation regions persist in FLs during both systole and diastole ,as highlighted by the arrows in Figures 1.13 and 1.14. These are consistent with the rotating streamlines visible in Figures 1.10 and 1.11. Specifically, FPA exhibits a single significant stagnation point that involves the aortic arch FL (Figures 1.13b and 1.14b). The PTA has three dominant stagnation regions (Figures 1.13c and 1.14c): two in the aortic arch FL and one in the upper portion of the abdominal FL. The FTA exhibits 25 fragmented vortex structures and a single stagnation point located in proximity of O_8 (Figures 1.13d and 1.14d).

The intensity of T is generally higher at diastole than at systole in all geometries. In the HA, $T > 70\%$ mainly in the aortic arch (Figure 1.16a), consistent with the streamlines pattern in Figure 1.11 and the Q contours in Figure 1.14. At the systolic peak, maximum T is approximately equal to

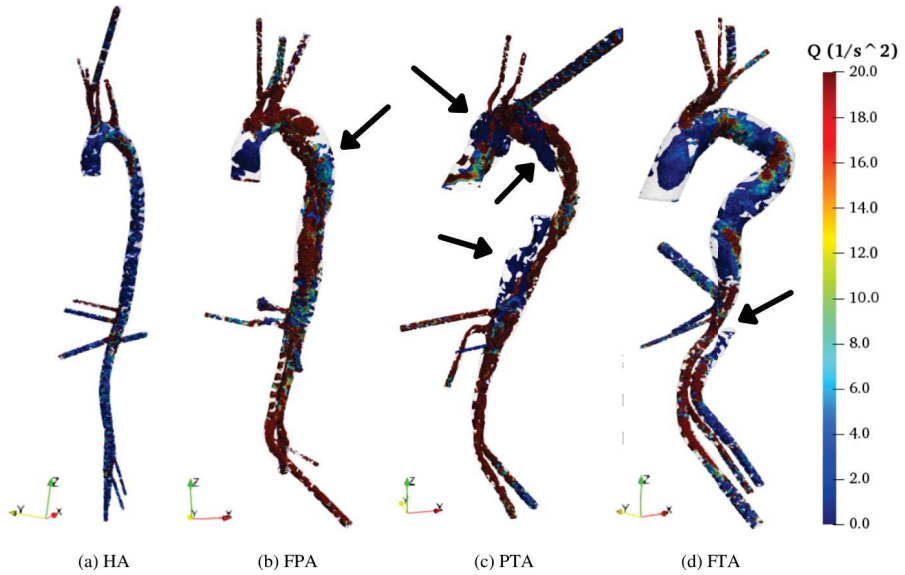

Figure 1.14: *Q contour plots at $t = 0.5\,\mathrm{s}$ (diastole). Grey colour represents $Q < 0$, which are not significant [102]. Black arrows identify relevant stagnation regions.*

40% in the ascending aorta. Small regions at higher values are located at the roots of the upper arteries. In dissected aortas, the region at $T > 70\%$ is more extended than in HA, both at systole (Figure 1.15) and diastole (Figure 1.16). In the FPA, the region at higher T is located downstream the tear in FL at systolic peak (Figure 1.15b), and upstream the tear in the aortic arch at diastole (Figure 1.16b). In the PTA, the high T region is more distinctly observed at systolic peak (Figure 1.15c) than in the other models. Figure 1.15c also shows high T regions ($\geq 80\%$) in proximity of the tears in the aortic arch and abdominal FLs. Such regions correspond to the abrupt TL restrictions. Unlike other geometries, the FTA displays high T also below the abdominal branches (O_{11}) (Figures 1.15d and 1.16d).

Our results demonstrate that the tears are major sources of highly turbulent flow, as is also clearly visible in Figure 1.12. For instance, Figures 1.12(c.2,d.2) show that the volume flow rate through O_8 drastically drops due to the stagnating flow region. Stagnation is generated therein by the specific geometry of the FL (the top thrombosed FL is three to five FL diameters above O_8) as well as by the relative position of O_8 and the tear (O_8 is approximately two FL diameters above the tear). In FPA and FTA, the flow through the tears is directed from the TL to the FL. Conversely,

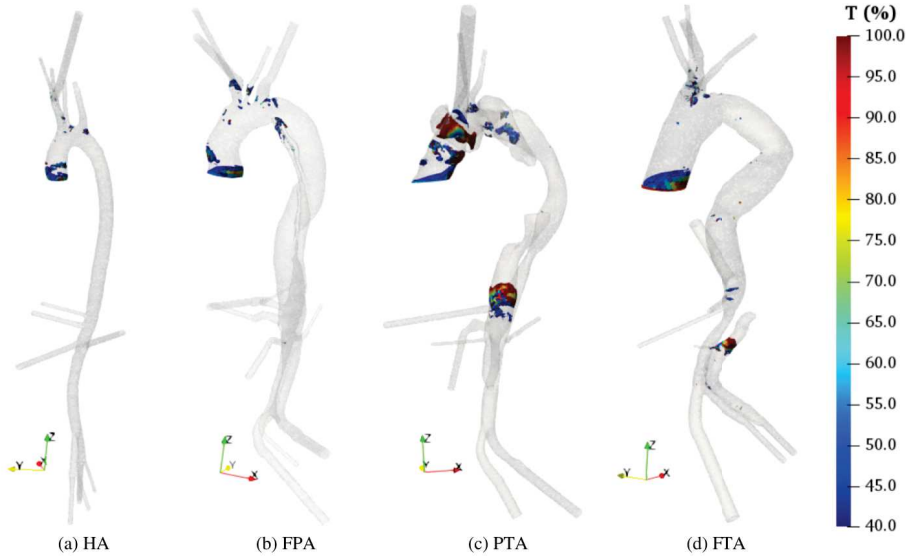

Figure 1.15: *T contour plots at $t = 0.15\,\mathrm{s}$ (systolic peak). The figure reports $T > 40\%$ to improve visualization.*

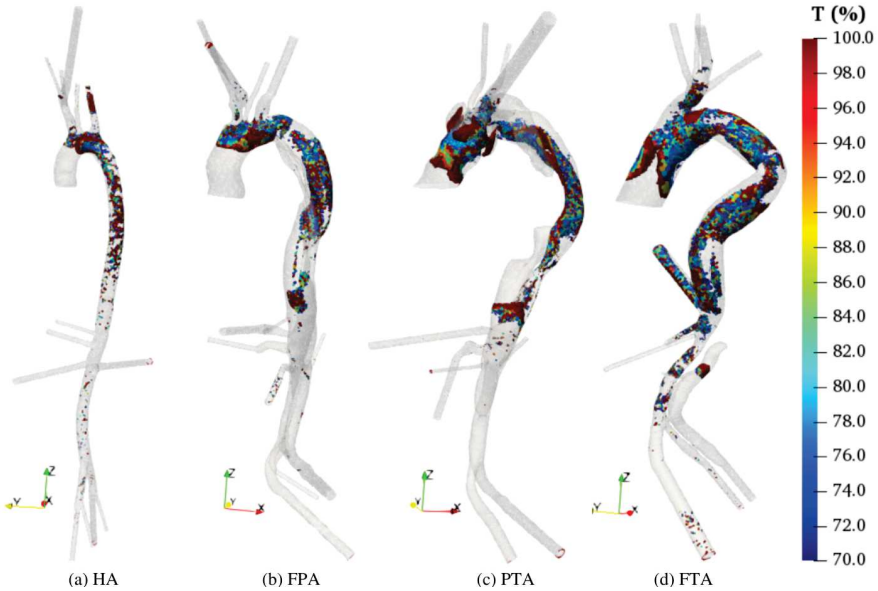

Figure 1.16: *T contour plots at $t = 0.5\,\mathrm{s}$ (diastole). For clarity, the figure reports only $T > 70\%$.*

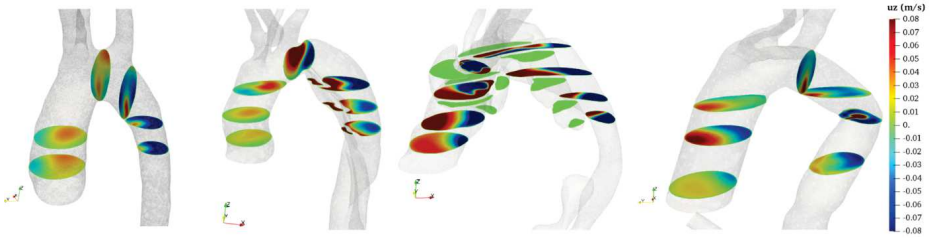

(a) HA (b) FPA (c) PTA (d) FTA

Figure 1.17: *u_z contour plots at $t = 0.5\,\mathrm{s}$ (diastole). Negative values indicate backflow in the ascending aorta.*

in the PTA, the FL bidirectionally communicates with the TL. Since the descending FL is thrombosed, the aortic arch FL feeds the TL upstream the thrombus (Figure 1.12b). As in the other geometries, the abdominal FL is instead fed by the TL.

To further explore flow kinematics, we report results for u_z at diastole in Figure 1.17. Such a flow pattern is generally more complicated than at systole due to the retrograde flow in ascending aorta (Figure 1.11). Retrograde flow is well evidenced by the u_z contour plot in Figure 1.17, whereby negative values in the ascending aorta represent backflow. In the HA (Figure 1.17a) and FPA (Figure 1.17b), the pattern is similar. As expected, in the FPA aortic arch, u_z is higher than in other models due to the TL restriction in proximity of the tear. In the PTA, u_z is also high in the ascending aorta (Figure 1.17c), while it is null for a large part of the FL due to geometric constraints. Positive u_z values in the descending aorta are a consequence of the vortexes evidenced at diastole in Figure 1.11.

1.4.3 Hemodynamic Forces

Hemodynamic forces are related to pressure and WSS. The pressure is higher when the flow acceleration is maximum (i.e., at $t = 0.1\,\mathrm{s}$) for all considered cases. In the HA and the FTA, the pressure is higher at the inlet and reduces towards the outlets for $0.05\,\mathrm{s} < t < 0.15\,\mathrm{s}$ (i.e., when the blood flow accelerates), while it has an opposite pattern for $0.2\,\mathrm{s} < t < 0.4\,\mathrm{s}$ (when the flow decelerates). On the contrary, in the FPA and PTA, the pressure reduces through the aorta also for a large part of the flow deceleration (i.e., for $0.05\,\mathrm{s} < t < 0.3\,\mathrm{s}$) due to the larger pressure drop, see the supplementary movies. In fact, in the FPA and PTA,

restrictions increase the average velocity and, thus, the friction pressure losses. Moreover, vortexes identified in Figure 1.11 for dissected aortas are additional sources of pressure drop. In general, these considerations highlight a different balance between fluid inertia and viscous forces among the different pathologies. Specifically, for HA and FTA, inertia dominates, whereas friction dominates for FPA and PTA.

Figure 1.18 shows that greater p values locate in the ascending aorta and aortic arch (in agreement with [49]). Moreover, in FPA and PTA, p is significantly higher than in HA and FTA, reaching 150 mmHg for the PTA FL and 130 mmHg for the FPA. FPA and PTA have greater velocity at the iliac arteries (see Figure 1.10). As a consequence, in these cases, the flow back-pressure is higher, increasing the outlet pressure also for all the other branches. Specifically, the average outlet pressure is approximately 50% and 40% higher compared to the HA, for all the outlets in FPA and PTA, respectively. Conversely, in the iliac branches of the FTA, the velocity is lower compared to the HA and, in turn, the flow back-pressure is reduced by 40%. In fact, the thrombosed FL acts as a stenosis on the TL, thus reducing the distal blood flow.

We compute the average pressure drop in the cardiac cycle as $< \mathcal{P}_I - \mathcal{P}_{O_{13}} > \simeq 1.6\,\text{mmHg}$ for the HA, 4.2 mmHg for the FTA, 7.3 mmHg for the FPA, and 20.8 mmHg for the PTA. Note that the pressure variation for the PTA is about 13 times higher compared to the HA. This probably explains the fact that PTA FL is more prone to aneurysmal degeneration and, ultimately, to aortic rupture [49]. In fact, in addition to greater pressure variations, diseased aortic walls have lower elasticity and, thus, more likely experience irreversible expansion. A preventive treatment of PTA FL may consist of surgically reaching complete FL thrombosis.

Pressure drop along the aorta derives from WSS and turbulent dissipation in vortex regions. In particular, according to [37], we evaluate the time-averaged WSS (TAWSS):

$$\text{TAWSS} = \frac{1}{\mathcal{T}} \int_0^{\mathcal{T}} \text{WSS}\, \mathrm{d}t\,, \tag{1.11}$$

as an indicator of the total stress on the aortic wall for a complete cardiac cycle. In all models, TAWSS is large at the carotids and subclavian roots (Figure 1.19) where the flow section narrows, the velocity increases (Figures 1.10 and 1.11), and the branch root acts as a flow obstacle. Except for such regions, in the HA, TAWSS is generally less than 2 Pa. Among

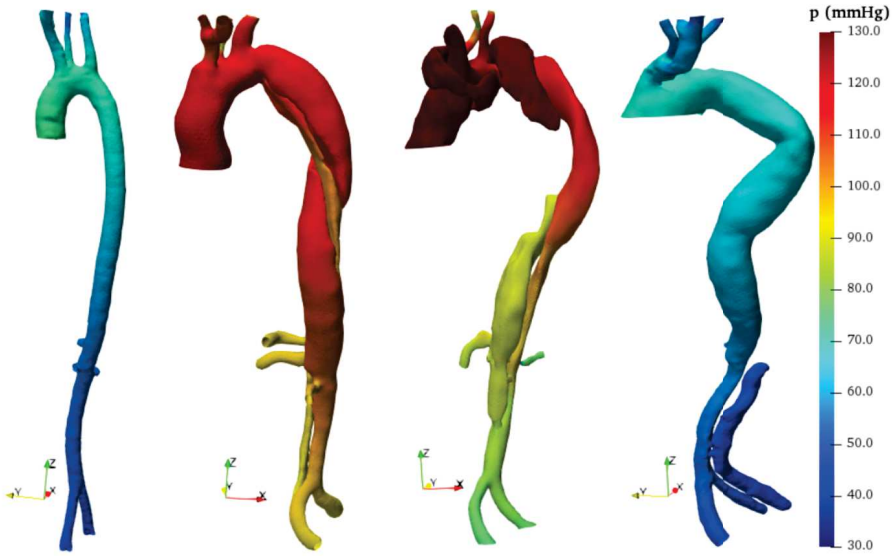

Figure 1.18: *Pressure contour plots at* $t = 0.1\,\mathrm{s}$ *(acceleration phase).*

dissected models, FTA has the lowest TAWSS pattern; however, moderate TAWSS values (i.e., $\simeq 2\,\mathrm{Pa}$) are detected in the abdominal TL, and greater values ($> 2\,\mathrm{Pa}$) are found close to the tears of the abdominal FL due to the high velocities of the jet-like flow (see Figures 1.12 and 1.19d). Notably, the literature identifies such areas of communication between TL and FL as potentially problematic spots [100].

In the PTA, TAWSS $> 2\,\mathrm{Pa}$ for the majority of the TL (Figure 1.19c), including the iliac arteries. Similar to the FTA, the jets through the communication tears between TL and FL generate high-TAWSS regions in the abdominal FL. However, the descending and aortic arch FLs exhibit the lowest TAWSS values due to the low velocity field and flow stagnation (see Section 1.4.2). High TAWSS values can also be observed in the FPA. Namely, TAWSS in the descending TL of the FPA is large due to the reduced flow area and consequently large velocity (Figure 1.19b). Similar values are detected close to the main tear in the TL aortic arch. Conversely, the FPA FL is characterized by relatively low TAWSS. However, its value increases along the abdominal FL and iliac arteries. In fact, as stated in Section 1.4.1, in O_{15} and O_{16}, the volume flow is significantly larger compared with the other geometries.

Comprehension of the pathology evolution can further benefit from

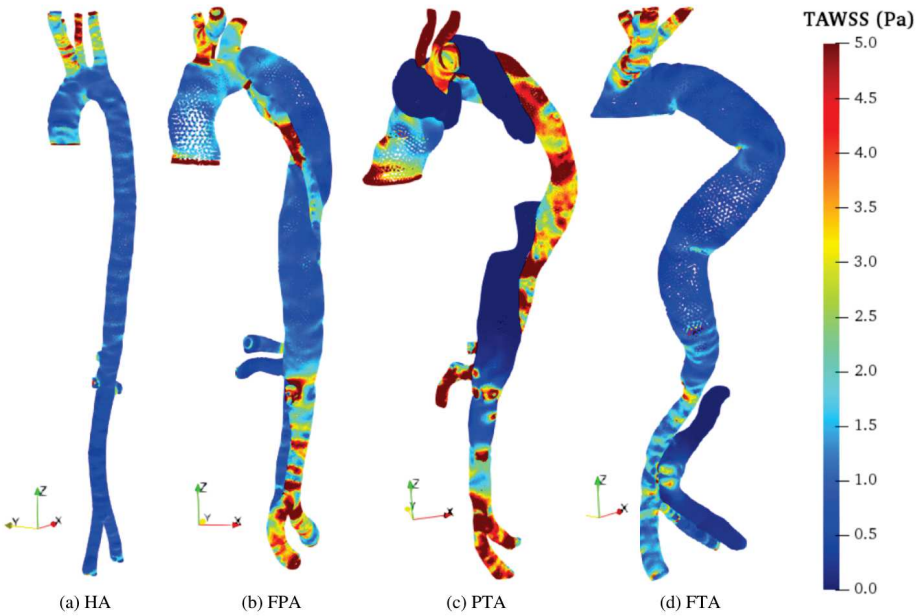

Figure 1.19: *TAWSS contour plots.*

evaluation of WSS dynamics [37, 76, 95]. Specifically, despite low TAWSS, vortex flow regions could be prone to aneurysm formation [37] as a consequence of stress oscillation that elicits structural fatigue. The oscillatory shear index (OSI) evaluates such unsteady WSS effects [37, 39]:

$$\mathrm{OSI} = \frac{1}{2}\left(1 - \frac{\left|\frac{1}{\mathcal{T}}\int_0^{\mathcal{T}} \overrightarrow{\mathrm{WSS}}\,\mathrm{d}t\right|}{\frac{1}{\mathcal{T}}\int_0^{\mathcal{T}} \mathrm{WSS}\,\mathrm{d}t}\right). \tag{1.12}$$

By definition, $0 \leq \mathrm{OSI} < 0.5$, and extended regions where OSI is close to 0.5 identify possible aneurysm formation [95].

In HA, high-OSI regions have limited extension and are generally disconnected along the abdominal aorta. Among all diseased models, the PTA exhibits the largest regions with high OSI (Figure 1.20c). Specifically, $\mathrm{OSI} \simeq 0.5$ for the whole aortic arch and within the upper portion of the abdominal FL, in the ascending aorta and aortic arch TL as well as where the FL merges into the abdominal TL. This is due to the presence of the stable vortex structures and stagnating flow already discussed in Secion 1.4.2. FPA shows the second most extended surface with $\mathrm{OSI} \simeq 0.5$, as reported in Figure 1.20b. In particular, critical regions comprise the

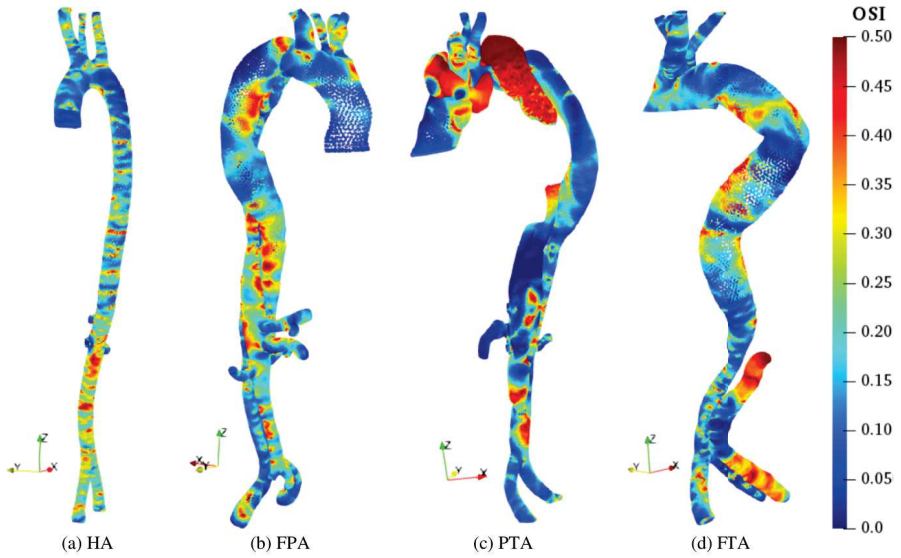

Figure 1.20: *OSI contour plots*

descending and aortic arch FL and the whole TL. This can be attributed to the stable helical (vortex) flow and the irregular FL surface. Finally, in the FTA, critical regions are consistent with the locations of the vortex structures identified in Section 1.4.2. Specifically, the high-OSI region in the upper portion of the abdominal FL corresponds to the stagnating flow. Furthermore, regions exhibiting periodic vortexes during diastole also have high OSI values. This is in agreement with findings in [103].

1.5 Summary

In this chapter, we provide new numerical evidence on the likelihood of degeneration in three types of aortic dissections (FPA type B/3, PTA type A/1, and FTA type B/3). We analysed patient-specific hemodynamics and compared them to a healthy aorta (HA) by combining CT-scan images and CFD. The results show altered flow kinematics for all the dissected aortas. In particular, the branches that originate from FLs or close to tears were poorly perfused. Compared to HA, the velocity of dissected aortas was higher in the abdominal aortic reach (both for TLs and FLs) and iliac arteries. At diastole, the streamlines showed complex flow patterns characterized by high T and vortexes not only in the ascending but, also in

the descending and abdominal aorta. According to the Q-criterion, several stagnation regions persist in all FLs and thus cause poor oxygenation that reduces the aorta wall resilience and increases the wall rupture risk [101, 104].

FPA FL and PTA TL exhibit the highest pressure and TAWSS values: these are prominent risk factors for aortic degeneration and, ultimately, wall rupture [49]. In these geometries, high volume flow rate at the iliac outlets causes pressure to increase by approximately 50% in the whole domain compared to HA. Moreover, in PTA, considerable pressure losses of approximately 20 mmHg during the cardiac cycle are induced by TL cross-section restrictions at the aortic arch.

Unsteady fluid forces effects further demonstrate that FPA and PTA dissections are more prone to adverse aortic evolution compared to HA. In fact, while high OSI values generally characterize all diseased geometries, the PTA and FPA exhibit the most extended coherent regions. In particular, in the PTA, the entire aortic arch FL has an OSI value close to 0.5. Since such an area also has low TAWSS values, it is more likely to experience aneurysm formation during diastole [37] and eventual subsequent rupture [104]. Conversely, the PTA FL shows low OSI values upstream from abdominal branches, thus suggesting the risk of thrombus formation [37, 39]. In this scenario, our study functions as an effective decision tool supporting prognostic and therapeutic strategies. In fact, inducing the FL thrombosis, as in FTA, may effectively reduce PTA risks. Notably, FTA hemodynamic patterns more closely approximate HA, and such geometry overall exhibits less critical pressure, TAWSS, and OSI values.

Our work provides useful guidelines for future analysis of aortic dissection with CFD. Specifically, we demonstrated that the y^+ value dominates the mesh sensitivity compared with surface grid density. Thus, $y^+ < 0.3$ should be selected to correctly evaluate the WSS. Moreover, validation highlights that the RANS modeling approach, with a low-Reynolds turbulent energy equation-based closure model without wall functions, correctly balances the computational burden and modeling accuracy, yielding coherent results within acceptable computational time.

The most relevant assumptions of this study are the rigid wall and Newtonian fluid hypotheses. Elastic walls absorb wall shear stress (WSS), thus reducing its value [49]. Further, following a rigid wall approach, the effects of lumen dilatation and collapse due to pressure fluctuations are neglected. These events increase the risk of end-organ ischemia, which is not

considered in our work. Nevertheless, the rigid wall assumption is widely accepted in the literature to (i) circumvent eventual uncertainties on the patient-specific wall biomechanical characteristics [39], and (ii) overcome computational costs of the fluid-structure interaction approach [56]. This study as well as numerous additional investigations [32, 39, 105–107] support the fact that the rigid wall assumption does not significantly influence aortic hemodynamic behavior, and that WSS distribution is comparable to simulation results obtained with the fluid–structure interaction approach. Regarding the Newtonian fluid assumption, we note that red blood cells cause shear thinning phenomena, where blood viscosity decreases under shear strain and high WSS values are thus reduced [108]. In the backflow phase, Newtonian models tend to overestimate the WSS and turbulent intensity [39, 109]. The risk of aneurysm formation and wall rupture may in turn be underestimated in such areas where WSS values are overestimated [110, 111]. Despite such criticalities, the Newtonian approximation is typically considered acceptable for large arteries, such as the aorta [112]. Generally, it is reasonable to assume a Newtonian fluid for large vessels (1–3 cm in diameter), healthy arteries and arterioles, as well as healthy veins and venules (0.2 mm–1 cm in diameter) [108]. The diameters of arteries in our models fall within those ranges spanning from 0.31 cm to 1.39 cm, and the diameter of aortas is approximately 3.5 cm. Although the number of patients included in this study is too small for statistical significance, we expect our methodology to improve in the prevention, diagnosis, and management of aortic dissection by suggesting favorable/adverse flow patterns for the dissection outcome. Further work should focus on extensively verifying such patterns for a larger number of patients. Another amelioration will entail consideration of the patient-specific circulatory system. In this study, Windkessel coefficients for all dissected geometries are consistent with those of the HA.

Chapter 2

FSI Simulation Validation of an Idealized Aorta Model

The aorta is multiphysics system where hemodynamics and wall structural mechanic are mutually influenced. A fluid-structure interaction approach is appropriate to describe the mechanical alterations suffered by the aortic wall in response to altered hemodynamic patterns. This Chapter demonstrates the validation of the simulated idealized aorta model with a fluid-structure interaction (FSI) model through modified PIMPLE solver to use Robin-Neumann partitioned approach for the strongly-coupled algorithm. The validation involves the comparison of streamlines, pressure, and displacements with in vivo measurements. The geometry is reconstructed from the healthy aorta presented in Chapter 1.

Our analysis shows that the streamlines and pressure pattern are comparable with the literature data acquired using rich medical imaging data. The maximum diameter deformation at the level of abdominal aorta is comparable with measured data and the diameter deformation profile along the cardiac cycle correctly follow the velocity profile. According to this results, our work shows a high-performance simulation suitable for several future works.

The Chapter is organized as follows. In Section 2.1 the idealized model of the healthy aorta is presented and the physic model is described. The geometry models used and the numerical modeling methodology are accurately described in Section 2.2. Section 2.2 is divided in Sub-Sections to present fluid model (sub-section 2.2.2.1), solid model (Sub-section 2.2.2.2), fluid-solid coupling model (sub-section 2.2.2.3), boundary conditions (sub-

section 2.2.2.4), and mesh model (sub-section 2.2.2.5). Convergence and mesh sensitivity are studied in section 2.3. In section 2.4 the simulation results are presented and the validation is verified. Section 2.5 summarizes the main findings from the present Chapter.

2.1 Problem Statement

The aim of this Section is to describe the equations governing the physics of the system and the idealized model of the healthy aorta.

We reconstruct the idealized aorta (IA) model (Figure 2.1) based on the model of the healthy aorta presented in the Chapter 1.

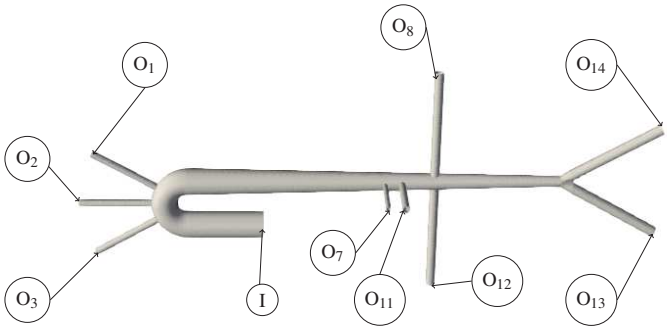

(a) IA

ID	Artery name
I	Inlet
O_1	Left subclavian
O_2	Left common carotid
O_3	Right common carotid
O_4	Right subclavian
O_5	Right internal common carotid
O_6	Anonymus
O_7	Celiac
O_8	Left renal
O_9	Splenic
O_{10}	Epatic
O_{11}	Superior mesenteric
O_{12}	Right renal
O_{13}	Right common iliac
O_{14}	Left common iliac

(b)

Figure 2.1: *Representation of the aorta model: (**a**) IA model with relative arteries; (**b**) names of the branches.*

We assume the same hypothesis for blood and flow, and the same orthogonal Cartesian reference reported in section 1.1. The flow is modeled by the following Navier–Stokes (N-S) equation (Equation (2.1)) and mass conservation equation (Equation (2.2)) which can be written in the Arbitrary Lagrangian-Eulerian (ALE) form as follows [63, 113]:

$$\rho_f[\frac{\partial \vec{u}_f}{\partial t} + (\vec{u}_f + \vec{u}_m) \cdot \nabla \vec{u}_f] = -\nabla p + \nabla \cdot \vec{\tau} \tag{2.1}$$

$$\nabla \cdot \vec{u}_f = 0\,, \tag{2.2}$$

$$\vec{\tau} = \mu[\nabla \cdot \vec{u}_f + (\nabla \cdot \vec{u}_f)^T]\,, \tag{2.3}$$

where t is time, $\vec{u}_f = (u_x, u_y, u_z)$ is the fluid velocity field, $\vec{u}_m = (u_x, u_y, u_z)$ is the velocity of mesh, p is pressure, $\mu = 3.71 \times 10^{-3}\,\mathrm{kg/m\,s}$

is the dynamic viscosity [67], $\vec{\tau}$ is the shear stress tensor, and $\rho_f = 1060\,\mathrm{kg/m^3}$ the blood density [48].

The deformations and displacements are small therefore Lagrangian approach is adopted for the solid analysis in FSI [113]. Linear elastic equations for the structure in Lagrangian form are written as follows [114]:

$$\rho_s \frac{\partial^2 \vec{D}}{\partial t^2} = \nabla \cdot \vec{\sigma} + \vec{b}\,, \tag{2.4}$$

$$\vec{\sigma} = \vec{C} : \vec{\epsilon}, \tag{2.5}$$

$$\vec{\epsilon} = \frac{1}{2}[(\nabla \vec{D}) + (\nabla \vec{D})^T]\,, \tag{2.6}$$

where $\rho_s = 2000\,\mathrm{kg/m^3}$ [115] is a solid density, $\vec{b}$ is the body force per unit mass, $\vec{\sigma}$ is the Cauchy stress tensor, $\vec{\epsilon}$ is strain tensor, $\vec{D}$ is displacement vector, $\vec{C}$ is a fourth-order tensor representing linear elastic stiffness.

The aortic wall is a homogeneous, anisotropic, nonlinear hyperelastic material [116, 117] but to reduce the computational cost [118] and because there are not significant different in the velocity fields calculated [119], we assume the wall as an isotropic, linear, and elastic solid. Linear Hookean constitutive low is adopted to define $\vec{\sigma}$ [120] where $E = 1.5\,\mathrm{MPa}$ is Young′s Modulus [121] and Poisson ratio is $\nu = 0.3$, used for large artery as aorta [122, 123].

The effects of hemodynamics on the distribution of stress on the aortic wall are analysed in terms of Von Mises Stress [62]:

$$\mathrm{sigmaEq} = \sqrt{\frac{(\sigma_1 - \sigma_2)^2 + (\sigma_1 - \sigma_3)^2 + (\sigma_2 - \sigma_3)^2}{2}}\,, \tag{2.7}$$

where σ_1, σ_2, and σ_3 are the principal stresses.

2.2 Methods

2.2.1 Geometric Models for FSI Simulation

We have built several models to set FSI simulation parameters (Figure 2.2). The aim of this procedure is to choose the best FSI simulation parameters for fast convergence. All models have the same geometric characteristics, but have an increasingly complex geometry. For all models, the diameter is 3cm and the wall thickness is 2mm.

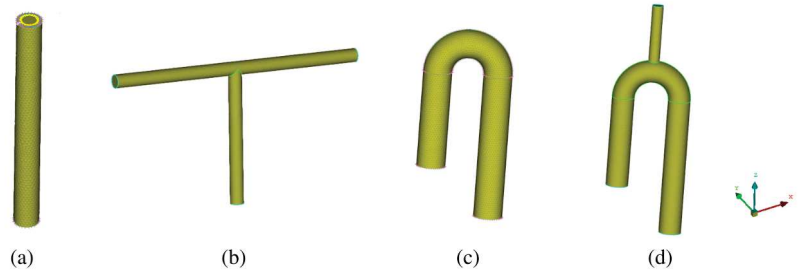

Figure 2.2: *Support models for optimizing FSI simulation parameters.*

We use the model 2.2a to study: (i) the effects of the wall layers numbers on the mesh sensitivity, (ii) the effect of the abdominal pressure (52.5Pa [57]) on the wall displacements, (iii) to choose the optimum parameters for simulation tolerances, and (iv) to analyse the effects of different constitutive lows, different values of Poisson ratio, Young′s Modulus, and wall density on the wall displacements.

The models 2.2b, c, and d are used to set the best boundary conditions. The IA model (see Figure 2.3a) is used to test the Robin BC and for FSI validation. This model is reconstructed with measurements obtained from the healthy aorta model presented in Chapter 1 and reported in Figure 2.3b.

Figure 2.3: *Aorta models for FSI validation: (**a**) IA model and (**b**) HA model presented in Chapter 1.*

The arteries are elongated with virtual cylinders to avoid the excessive proximity of the BCs to flow regions with significant gradients to cause numerical instability. The length of such cylinders is about 10 times the branch diameter.

2.2.2 Numerical Models

We use a partitioned FSI method to solve separately the fluid (Eq. 2.1, Eq. 2.2, and Eq. 2.3) and solid (Eq. 2.4, Eq. 2.5, and Eq. 2.6) governing equations. We use toolbox solids4foam-v2.0 [124] for performing fluid-solid interaction simulations implemented in the software package OpenFOAM-v9 [125].

Numerical simulations are performed using parallel computing through the public domain openMPI implementation of the standard message passing interface (MPI) [83]. We used the Scotch decomposition method for domain partitioning (20 sub-domains). Parallel computing are performed on 20 Intel® Xeon® E5-2680-v2-@-2.80 GHz processors and took 60 h. Equivalently, the velocity update was 192,000 nodes per second.

2.2.2.1 Fluid Model

We use the RANS [76–78] approach to numerically solve Equations (2.1) and (2.2) in their Reynolds-Averaged form. We assume the Launder and Sharma $k-\varepsilon$ turbulence model [79] to describe sub-grid stresses. In fact, this model is suitable to solve the low Reynolds number phenomena [79, 80] (e.g., where the non-dimensional wall distance in wall units is small, $y^+ < 5$ [78]) relevant in the aortic blood flow, which is in the transitional regime [76]. Specifically, it does not use any wall functions to solve the boundary layer [80], allowing a reliable evaluation of the WSS [81]. Such a closure model introduces three variables (k; the turbulent kinetic energy dissipation rate, ϵ; and the turbulent viscosity, ν_t) and the relative transport equations. The mathematical equations of the model presented in Section 2.1 are discretized using the cell-centred finite volume method [113] with collocated variable arrangement [82]. The Pressure-Implicit with Splitting of Operators (PISO)–Semi Implicit Method for Pressure-Linked equations (SIMPLE) algorithm [77, 84] (PIMPLE) solves the pressure–velocity coupling and the non-linearity in Equations (2.1) and (2.2). The Euler implicit scheme [85] is selected for temporal integration. The Gauss linear scheme is used for the spatial interpolation of the gradients for fluid. The convective terms of Equations (2.1) and (2.2) are interpolated with the Gauss linear schemes [82]. Similarly, the convective terms for the k and ϵ equations of the Launder and Sharma model are interpolated through the Linear Upwind scheme. The Geometric-Algebraic Multi-Grid (GAMG) iterative algorithm is used to solve the linear system of equations obtained from temporal and spatial discretization of the pressure equation, while the iterative symmetric Gauss–Seidel method solves the linear systems of equations for u, k, and ϵ [70]. Tolerances for the values for fluid iterative linear system solvers are reported in Table 2.1.

Table 2.1: *Tolerance values for fluid iterative linear system solvers.*

Variable	Tolerance	Relative Tolerance
p/ρ	$10^{-6}\,\mathrm{m}^2/\mathrm{s}^2$	0.01
u	$10^{-6}\,\mathrm{m}/\mathrm{s}$	0.05
k	$10^{-6}\,\mathrm{m}^2/\mathrm{s}^2$	0.05
ϵ	$10^{-6}\,\mathrm{m}^2/\mathrm{s}^3$	0.05
ν_t	$10^{-6}\,\mathrm{m}^2/\mathrm{s}$	0.05

The velocity Laplacian solver [126] is used to control deformation and morphing of the fluid mesh during the simulation with Quadratic Inverse Distance method for diffusivity [127].

2.2.2.2 Solid Model

The solid Equations (Eq. 2.4, Eq. 2.5, and Eq. 2.6) are solved according to the method reported in [113] for the case of linear geometry models. The segregated algorithm is used to solve the linear system of algebraic equations obtained from the discretized solid model [64] where the solution vector is displacement increments (DD) [113]. The Euler implicit scheme [85] is selected for temporal integration. The second-order accurate three time-level implicit scheme is used for solid gradient [77]. The Preconditioned Conjugate Gradient (PCG) iterative algorithm is used to solve the linear system of solid algebraic equations [113, 125].

We assess the tolerance value for solid iterative linear system solvers comparing magnitude of point displacement of different simulations. The aim of this analysis is the reduction of convergence time. The model used is represented in Figure 2.2a. The error is calculated through Equation 2.8:

$$\Delta_{\mathrm{mag(D)}} = \frac{1}{N_s} \sum_{l=1}^{N_s} \frac{\left| \mathrm{mag(D)}_j(t(l)) - \mathrm{mag(D)}_m(t(l)) \right|}{\max\left[\mathrm{mag(D)}(t(l))\right] - \min\left[\mathrm{mag(D)}(t(l))\right]}\,, \tag{2.8}$$

where j and m identify the different simulations with different tolerance values, $mag(D)$ is the magnitude of point displacement $\vec{D}$. We consider $\Delta_{\mathrm{mag(D)}} < 5\%$ acceptable, whereby the tolerance values is 5×10^{-4} m and the relative tolerance is 0.1.

The Lagrangian approach to the equations of the solid does not involve updating the single points of the solid mesh, so a dynamic solver is not required [127].

2.2.2.3 Fluid-Solid Coupling Model

The Robin-Neumann scheme [63–65, 128] is used for strongly-coupled algorithm to perform iterations between the fluid and solid solvers in FSI [64]. The PIMPLE solver in solids4foam does not include the RN scheme, so we modified it. The new code is reported in Appendix B. The interface interpolation procedure is Arbitrary Mesh Interface (AMI) [129]. Fixed

relaxation is used to accelerate the convergence [63, 113, 130, 131] and the relaxation factor is 5×10^{-5}. The tolerance for the FSI loop within each time-step is 0.1. The time-step length is 0.001 and the time-stepping strategy is Co-dependent. The maximum value of Courant number is 0.5.

2.2.2.4 Boundary Conditions

Table 2.2 summarizes the mathematical formulation for all the boundary conditions (BCs). In particular, a velocity inlet type BC approximates the flow that leaves the heart entering the computational domain through surface I (see the inlet identifiers in Figure 2.1). Specifically, $u_0(t)$ in Equation 1.9 is reported in Figure 1.5a. Therein, points are sampled from [48], where $u_0(t)$ was obtained through in vivo PC-MRI of the ascending aorta root. We use a Fast Fourier Transform (FFT)[86] to interpolate such discrete measures to the continuous periodic function also depicted in Figure 1.5a. The correlation coefficient is $R^2 = 0.999$ assuming 8 modes and the parameters reported in Figure 1.5b. We note that the peak systolic velocity is about 0.5 m/s and the average inlet flow is about 6 l/min [87]. The duration of a cardiac cycle is $\mathcal{T} = 0.96\,\mathrm{s}$. The maximum Reynolds number is 4600. Note that to capture the flow kinematics during diastole, $u_0(t)$ allows backflow through I ($u_0(t) < 0$ in Figure 1.5), see also [88].

We use inlet-outlet type BCs for all the other permeable boundaries identified by $[\mathrm{O}_1 \dots \mathrm{O}_{13}]$ in Figure 2.1. Such BC automatically switches between inlet and outlet modeling as a function of the flow direction [89], see Equations infow (In) and outflow (Out) in Table 2.2. Therein, $p_{\mathrm{O}_i}(t)$ is determined through the 3-element Windkessel model (Equation (2.9), [90]) that simulates the resistance of the remaining vascular peripheral network [49, 91]

$$\frac{Q_{\mathrm{O}_i}(t)}{C} = \frac{\mathrm{d}(p_{\mathrm{O}_i}(t) - R_1 Q_{\mathrm{O}_i}(t))}{\mathrm{d}t} + \frac{1}{R_2 C}(p_{\mathrm{O}_i}(t) - R_1 Q_{\mathrm{O}_i}(t)) \ . \qquad (2.9)$$

In Equation (2.9), Q_{O_i} is the volume flow rate at the outlet O_i, C is the network compliance, R_1 is the proximal resistance, and R_2 is the distal resistance. We estimate the constants C, R_1, and R_2 following the procedure in [91] and reported in Appendix A. Equation (2.9) is integrated in time through the Euler explicit method.

Robin BC (Equation 2.10) for pressure is set on the fluid-solid interface side-fluid (wall-fluid). This BC creates a link between stress, displacement

Table 2.2: *Mathematical description of the assumed boundary (B) conditions where $\hat{n}$ is the unit normal to the model surface.*

B	$\vec{u}$	p	k	ϵ	$\vec{D}$
I	$\vec{u} = u_0(t)\hat{n}$	$\frac{\partial p}{\partial \hat{n}} = 0$	$k = k(t_0)$	$\epsilon = \epsilon(t_0)$	$\vec{D}_n = 0$
$[O_1...O_{13}]_{In}$	$\frac{\partial \vec{u}}{\partial \hat{n}} = 0$	$p_{O_i}(t)$	$\frac{\partial k}{\partial \hat{n}} = 0$	$\frac{\partial \epsilon}{\partial \hat{n}} = 0$	$\vec{D}_n = 0$
$[O_1...O_{13}]_{Out}$	$\vec{u} = u_{O_i}$	$\frac{\partial p_{O_i}(t)}{\partial \hat{n}} = 0$	$k = k_{O_i}$	$\epsilon = \epsilon_{O_i}$	$\vec{D}_n = 0$
wall-fluid	$\vec{u} = 0$	Eq 2.10 [64]	$k = 10^{-10}$	$\epsilon = 10^{-10}$	$\vec{D}_f = \vec{D}_s$
wall-solid	$\vec{u} = 0$	$p_{abdominal} = 0$	–	–	–

and velocity [64, 132, 133]:

$$p^k + \frac{\rho_s h_s}{\rho_f}\left(\frac{\partial p}{\partial \hat{n}}\right)^k = p^{(k-1)} - \rho_s h_s \left(\frac{\partial \vec{u}}{\partial \hat{n}}\right)^{(k-1)} . \tag{2.10}$$

where k is the iteration counter, h_s is the virtual thickness and is calculated using propagation speed of p-waves in an elastic media. Since p-wave speed is infinite in the case of incompressible solid, virtual thickness is set to local thickness of the structure [65]. We estimate rhs, coeff0, and coeff1 value in the simulation as follow:

$$\text{rhs} = \rho_s h_s \,, \tag{2.11a}$$

$$\text{coeff0} = 1 \,, \tag{2.11b}$$

$$\text{coeff1} = \frac{\rho_s h_s}{\rho_f} \,. \tag{2.11c}$$

where $h_s = 0.002$m.

The conditions of displacement compatibility and traction equilibrium along the solid-fluid interfaces must be satisfied as follows [62]:

$$\vec{D}_f = \vec{D}_s \tag{2.12a}$$

$$\vec{\sigma}_f = \vec{\sigma}_s \tag{2.12b}$$

where $\vec{D}_f$ is the displacement applied to the fluid-side of wall-fluid, $\vec{D}_s$ is the displacement applied to the solid-side of wall-fluid, $\vec{\sigma}_f$ is the traction applied to the fluid-side of wall-fluid, and $\vec{\sigma}_s$ is the traction applied to the solid-side of wall-fluid.

On the external solid wall (wall-solid) the abdominal pressure is not applied. Analysis of the model in Figure 2.2a shows that the abdominal

pressure does not significantly affect the displacement results. Comparing two simulations with and without abdominal pressure applied on wall-solid, the error $\Delta_{\text{mag(D)}}$ is $< 0.38\%$ (Eq.2.8) and we consider it acceptable. The orthogonal displacement at the I and $[\text{O}_1 \dots \text{O}_{13}]$ surfaces is zero ($\vec{D}_n = 0$), but the two displacement tangential directions are free, i.e. the wall can contract and expand.

We initialize the domain assuming $p(t = 0) = 0$, $\vec{u}(t = 0) = \vec{0}$ and $\vec{D}(t = 0) = \vec{0}$. We then estimate the turbulent flow variables as:

$$k(t_0) = \frac{1}{2} \max \left[(u_0(t))^2 \right] , \tag{2.13a}$$

$$\epsilon(t_0) = \frac{C_\mu^{0.75} k^{1.5}}{L} , \tag{2.13b}$$

$$\nu_t(t_0) = \rho C_\mu \frac{k^2}{\epsilon} \tag{2.13c}$$

where $L = 0.038D$ is the reference length scale [85], and $C_\mu = 0.09$ [79].

2.2.2.5 Mesh Model

We use an unstructured meshing approach for surface and volume through the ANSA v.21.1.2 software. The procedure for fluid mesh is described in Section 1.2.2 (Figures 2.4a and 2.4b). The solid mesh is structured like the real aorta wall with three layers. The thickness of the wall is 2 mm and the thickness of intima, media, and adventitia layers are 0.2 mm, 1.2 mm, and 0.6 mm respectively [134]. The mesh of intima and adventitia are discretized using structured mesh algorithm, while the remaining volume is discretized using tetrahedra through the tetra-CFD algorithm with maximum growth factor of 1.1 (Figure 2.4c).

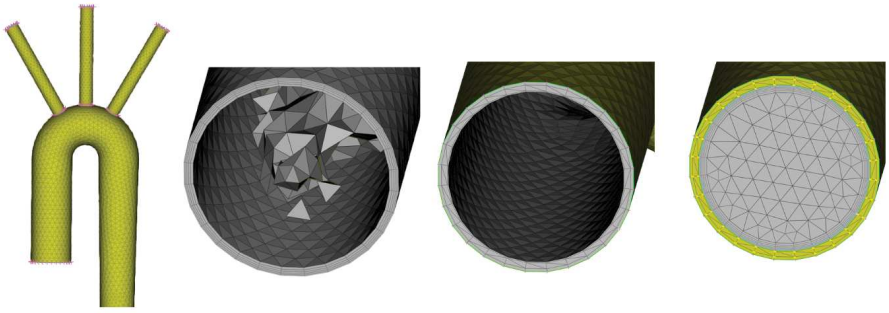

Figure 2.4: *Representation of the meshes. (**a**) surface mesh of the model; (**b**) tetrahedra fluid volume mesh and layers; (**c**) solid volume mesh with 3 layers for the wall. (**d**) Complete volume of the IA model: fluid (grey) and solid (yellow).*

2.3 Convergence and Mesh Sensitivity

The convergence and mesh sensitivity are guaranteed because the mesh is constructed with guidelines described in Section 1.3 of the Chapter 1. We analyse results of 4th cycle and consider the quality parameters showed in Section 1.3.2, i.e. the $y^+ < 0.3$. In Table 2.3 we report the mesh quality evaluated through its non-orthogonality, skewness, and aspect ratio. In agreement with standard procedures in CFD for optimal solution convergence and high solution quality, the non-orthogonality is lower than 65 and the skewness is lower than 4.

Table 2.3: *Relevant quality parameters for IA model.*

	fluid mesh	**solid mesh**
n surface elements	23,656	24,976
n polyhedra	259,695	122,861
Max non-orthogonality	54.18	60.56
Max skewness	2.7	2.18
Max aspect ratio	10.6	13.09
y^+	0.25	–
First-layer thickness	2%	–

We assess the impact of the layers number of solid mesh on the dis-

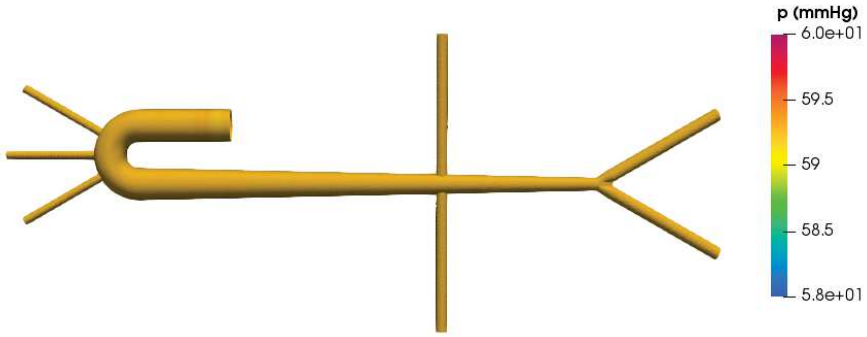

Figure 2.5: *Pressure at* $t = 0.15$s *(systolic peak).*

placements results. This aim at demonstrating the independence of the results from the solid grid. Analysis of the model in Figure 2.2a shows that a larger number of layers does not significantly affect the results. Comparing two models with walls of 3 and 6 layers, the error $\Delta_{\text{mag(D)}}$ is $< 1\%$ (Eq.2.8) and we consider it acceptable.

2.4 Results and Discussion

RN partitioned procedure ensures greater stability to the simulation because the pressure on the wall is limited by the wall inertia [64]. The fluid pressure is uniform on the wall-fluid (Figure 2.5) and the pressure pattern is coherent with the results obtained in [49]. The streamlines (Figure 2.6) at the systolic peak ($t = 0.15$s) and at diastole ($t = 0.5$s) have the same pattern of imaging data obtained by 3D Cine PC MRI measures reported in [88, 121, 135]. In the central portion of the ascending vessel the velocities are higher and the recirculation zones have been correctly simulated (see the portion indicated by black arrow in Figure 2.6a). Negative values in Figure 2.6b indicate backflow in the ascending aorta (see also the portion indicated by black arrow in Figure 2.6b where the central flow is contracted due to the presence of retrograde flow.).

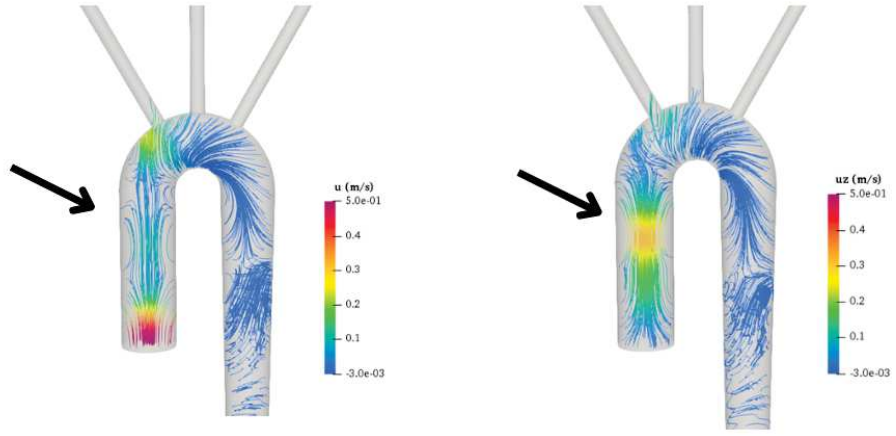

Figure 2.6: *Streamlines: (**a**) at $t = 0.15$s (systolic peak), (**b**) at $t = 0.5$s (diastole). The black arrows indicate the vortices and backflow respectively.*

Notably, the streamlines of the descending aorta are also consistent with the scheme observed in imaging data [49].

The Figure 2.7 shows the $mag(D)$ at $t = 0.15$s (systolic peak). The regions most prone to deformation (see Figure 2.9) are the ascending aorta, the descending aorta, and the abdominal aorta between the renal and iliac arteries. The displacements are of the order of the millimeters, consistent with the literature results [136, 137].

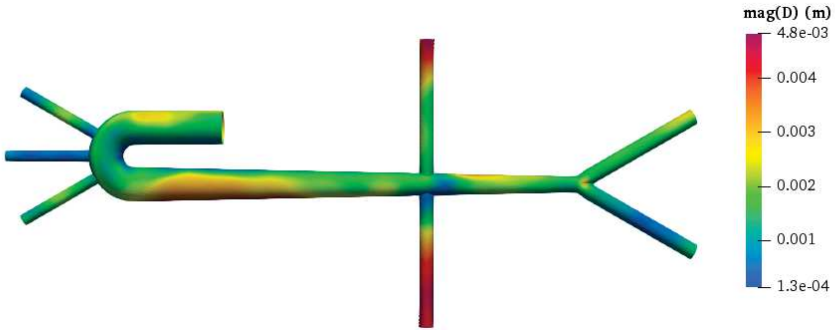

Figure 2.7: *Displacements at $t = 0.15$s (systolic peak).*

We have analysed the lumen diameter deformation in y-direction along

the cardiac cycle on a abdominal aorta section, orthogonal to z-axe. MRI phase contrast measurements [137] show a maximum deformation value of 4mm, while in our simulation this value is 5.5mm (see Figure 2.8). The maximum deformation difference between the simulation results and the MRI measurements is present also in [137] and is about 2mm and it can be due to the underestimation of the hydrostatic pressure applied on the external wall [137]. The profiles of lumen diameter deformation are different in the two compared works, but have the same trend along the cardiac cycle of the velocity profile respectively assigned. Figure 2.8 shows the vessel dilation at the systolic peak ($t = 0.15$s) and the contraction at the beginning of the diastole ($t = 0.4$s). Specifically, the expansion occurs when the velocity profile assumes positive values and the contraction where the velocity is negative (see Figure 1.5a of Chapter 1). The vessel dilation is probably caused by the presence of flow vortices highlighted by the streamlines (see Figure 2.6).

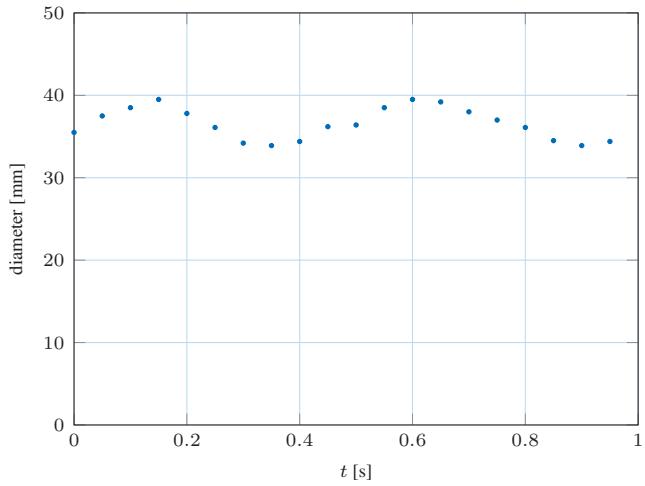

Figure 2.8: *Lumen diameter deformation along the cardiac cycle at abdominal aorta.*

Figure 2.9 shows the wall region where the deformations are high. Research has shown that displacements are not significant for the study of the disease degenerations, but the stress must be analysed. Therefore, we report in Figure 2.10 the Von Mises stresses.

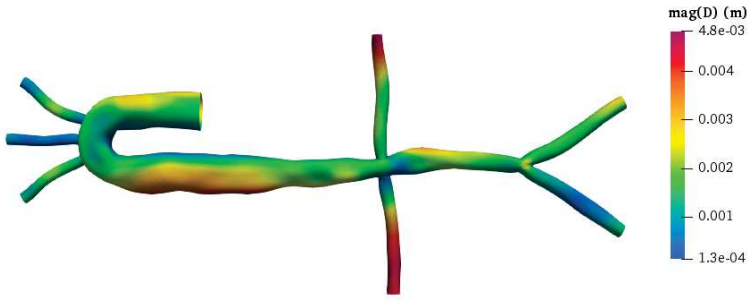

Figure 2.9: *Deformed model at* $t = 0.15$s *(systolic peak). The displacements have been multiplied by* 5 *to highlight the deformed configuration.*

The Von Mises Stress is high at the aortic arch and reach the highest value at the systolic peak (see Figure 2.10).

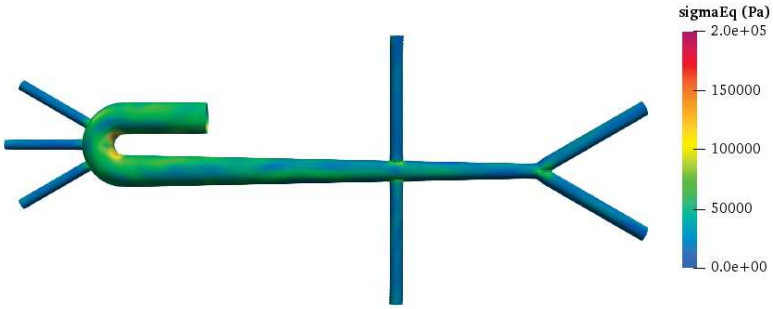

Figure 2.10: *Von Mises Stress at* $t = 0.15$s *(systolic peak).*

The high stress values are located in the aortic arch and the maximum values is about 140000Pa and is lower than the limits required by the biomechanical tests [61], as expected for a healthy aorta.

2.5 Summary

This Chapter validates a fluid-structure interaction simulation of an idealized healthy aorta model. Specifically, we use a Robin-Neumann partitioned approach for fluid-solid coupling model. RN scheme takes into account the inertia of the solid wall and limits the pressure values that cause improper wall displacements and simulation instability [64]. We have modified the PIMPLE solver in solids4foam so that it could solve

RN scheme and we report the code in Appendix B. We compare the results with imaging data measurements presented in literature and find a great similarity. The streamlines show the flow recirculation zones in the ascending aorta and the backflow during diastole [88, 121, 135]. The chaotic motion in the descending aorta, also visible in MRI measurements in [49], is correctly simulated. The maximum lumen diameter deformation along the cardiac cycle is 5.5mm and is comparable with the result obtained by Reymond in [137]. Finally, being the analysis of a healthy aorta, the Von Mises stress pattern shows lower maximum value than failure limits [61]. The data of this research is available at the link: https://doi.org/10.5281/zenodo.7995669. The most relevant assumptions of this study are linear and isotropic elastic material and Newtonian fluid hypotheses to reduce the computational cost. Specifically, linear constitutive law may not accurately assess wall stress [137]. Therefore, it would be desirable in future works to test the results assuming a hyperelastic aortic wall and specify the mechanical characteristics for each layer of the wall [62]. Regarding the Newtonian fluid hypotheses, we refer to Section 1.5 in which the implications of the choice are widely discussed. Future works may concern the application of this methodology to the patient-specific aortas presented in Chapter 1 and to compare the results with those obtained with standard CFD simulations.

Conclusions

This thesis studies the hemodynamics and the fluid-structure interaction of one idealized aorta, one healthy aorta, and three dissected aortas through two different computational approaches.

Chapter 1 provides useful guidelines for future analysis of aortic dissection and studies the flow distribution, the kinematics, and the hemodynamic forces in four patient-specific aorta models with CFD. The guidelines involve the following steps: (i) the geometric reconstruction through an ad hoc developed and minimally supervised image analysis procedure from CT scan, (ii) the selection of $y^+ < 0.3$ value, to correctly evaluate the WSS, i.e. WSS dominates the mesh sensitivity, and (iii) the selection of RANS modeling approach, with a low-Reynolds turbulent energy equation-based closure model without wall functions, because it reasonably balances the computational burden and modeling accuracy, yielding coherent results within acceptable computational time. The flow patterns in the fully perfused, partially thrombosed, and fully thormbosed aorta dissection are analysed and compared with a healthy aorta. The results show that partially thrombosed FL is more likely to degenerate and that there are different situations of disease degeneration. The ischemia risk of the organs connected to the branches that originate from FLs or close to tears is greater because they are poorly perfused. Aneurysm formation during diastole is increased by low TAWSS and the risk of thrombus formation is caused by low OSI. The wall rupture risk is increased by the presence of several stagnation regions, high pressure and OSI's limit value. Specifically, the FPA and PTA show a pressure increment by approximately 50% in the whole domain compared to HA, while PTA has an OSI value close to 0.5. The limitations of this study are the rigid wall and Newtonian fluid assumption. The rigid wall assumption is widely accepted by the literature and numerous studies [32, 39] support that rigid wall does not significantly influence aortic hemodynamic behaviour. Regarding the

Newtonian fluid hypotheses, it is reasonable to assume this behaviour for large arteries, such as the aorta [112]. Our methodology could improve the prevention and diagnosis of the aortic dissection, further verification is advisable on a large number of patients in future works.

Chapter 2 presents the validation of fluid-structure interaction simulation for idealized healthy aorta model. We use the Robin-Neumann partitioned approach for strongly-coupled algorithm to perform iterations between fluid and solid solvers. The RN scheme limits the pressure exerted by the fluid on the wall and ensures convergent and fast simulations [64]. Our results show a great similarity to data obtained from imaging techniques reported in the literature. Specifically, the results show: (i) the presence of flow vortexes in the ascending aorta at systolic peak, (ii) the chaotic flow at the descending aorta, (iii) the backflow at the diastole, (iv) the uniform pressure pattern, and (v) the vessel contraction and dilatation, with displacements comparable with literature values. The Von Mises stress reaches peak levels at the aortic arch, but it is lower than failure limits. This result is expected, having performed the simulation with the conditions of a healthy aorta. The most relevant assumptions of this study are linear and isotropic elastic material to reduce the computational cost. We could further improve the methodology considering the hyperelastic material and the mechanical characteristics of each wall layers. The next step of this work is the application of FSI to the patient-specific aortas presented in Chapter 1.

Appendix A

Windkessel Model Implementation

We calculate the constants C, R_1, and R_2 of the Windkessel model following the procedure in [91]. Specifically, the proximal resistance R_1 is defined as

$$R_1 = \frac{\rho}{A} \frac{13.3}{(2r_i)^{0.3}}\,, \tag{A.01}$$

where A is area of O_i expressed in [mm^2] and r_i is the radius of O_i expressed in [mm]. Moreover, C is

$$C = \frac{4 \times 10^{-3}\,\mathrm{s}}{R_t}\,, \tag{A.02}$$

where the total resistance R_t reads

$$R_t = \frac{\bar{P}}{\bar{Q}}\,, \tag{A.03}$$

where $\bar{P}$ is the mean pressure calculated following [96] and $\bar{Q}$ is the mean flow rate through O_i. The values of $\bar{P}$ and $\bar{Q}$ are obtained from a preliminary CFD simulation where we assumed 0 back-pressure at the outlets. Finally, $R_2 = R_t - R_1$.

Tables A.01–A.04 summarize the values used in Equation 1.7 and Table A.05 summarize the values used in Equation 2.9.

Table A.01: *Three-element Windkessel model parameters for HA.*

Output	$\bar{Q}$ **[m³/s]**	$\bar{P}$ **[mmHg]**	R_1 **[kg/m⁴s]**	R_2 **[kg/m⁴s]**	C **[m⁴s²/kg]**
O_1	2.25×10^{-5}	105.4	2.36×10^{7}	6.02×10^{8}	2.86×10^{-9}
O_2	1.20×10^{-5}	98.9	4.28×10^{7}	1.05×10^{9}	1.63×10^{-9}
O_3	3.07×10^{-5}	98.9	9.21×10^{6}	3.47×10^{8}	5.03×10^{-9}
O_4	8.37×10^{-6}	99.9	4.76×10^{7}	1.54×10^{9}	1.12×10^{-9}
O_5	6.43×10^{-6}	92.2	6.48×10^{7}	1.85×10^{9}	9.37×10^{-10}
O_7	8.62×10^{-6}	97.8	3.41×10^{7}	1.48×10^{9}	1.18×10^{-9}
O_8	2.43×10^{-5}	95.8	4.08×10^{7}	4.85×10^{8}	3.40×10^{-9}
O_{11}	1.97×10^{-5}	97.5	1.66×10^{7}	6.43×10^{8}	2.72×10^{-9}
O_{12}	2.99×10^{-5}	95.4	9.39×10^{6}	4.16×10^{8}	4.21×10^{-9}
O_{13}	1.56×10^{-5}	96.9	1.47×10^{7}	8.13×10^{8}	2.16×10^{-9}
O_{14}	1.07×10^{-5}	96.9	2.33×10^{7}	1.19×10^{9}	1.48×10^{-9}
O_{15}	6.31×10^{-6}	96.9	4.08×10^{7}	1.98×10^{9}	8.84×10^{-10}
O_{16}	4.75×10^{-6}	96.9	5.03×10^{7}	2.64×10^{9}	6.65×10^{-10}

Table A.02: *Three-element Windkessel model parameters for FPA model.*

Output	$\bar{Q}$ **[m³/s]**	$\bar{P}$ **[mmHg]**	R_1 **[kg/m⁴s]**	R_2 **[kg/m⁴s]**	C **[m⁴s²/kg]**
O_1	1.05×10^{-5}	105.4	2.25×10^{7}	1.32×10^{9}	1.33×10^{-9}
O_2	2.74×10^{-6}	98.9	8.87×10^{7}	4.73×10^{9}	3.72×10^{-10}
O_3	7.78×10^{-6}	99.7	2.33×10^{7}	1.68×10^{9}	1.05×10^{-9}
O_4	5.91×10^{-6}	99.9	5.84×10^{7}	2.19×10^{9}	7.95×10^{-10}
O_8	6.57×10^{-6}	95.8	3.84×10^{7}	1.91×10^{9}	9.21×10^{-10}
O_9	2.66×10^{-6}	93.4	2.46×10^{7}	4.66×10^{9}	3.82×10^{-10}
O_{10}	6.69×10^{-7}	97.3	1.26×10^{8}	1.93×10^{10}	9.24×10^{-11}
O_{11}	2.66×10^{-6}	97.5	5.35×10^{7}	4.84×10^{9}	3.66×10^{-10}
O_{12}	1.82×10^{-6}	95.4	9.88×10^{7}	6.90×10^{9}	2.56×10^{-10}
O_{13}	2.69×10^{-6}	96.9	6.59×10^{7}	4.74×10^{9}	3.72×10^{-10}
O_{14}	2.52×10^{-6}	96.9	6.89×10^{7}	5.06×10^{9}	3.49×10^{-10}
O_{15}	2.62×10^{-5}	96.9	1.53×10^{7}	4.78×10^{8}	3.63×10^{-9}
O_{16}	2.93×10^{-5}	96.9	1.55×10^{7}	4.25×10^{8}	4.06×10^{-9}

Table A.03: *Three-element Windkessel model parameters for PTA model.*

Output	$\bar{Q}$ [m^3/s]	$\bar{P}$ [mmHg]	R_1 [kg/m^4s]	R_2 [kg/m^4s]	C [m^4s^2/kg]
O_2	1.44×10^{-5}	98.9	9.27×10^{7}	8.25×10^{8}	1.95×10^{-9}
O_3	1.57×10^{-4}	98.9	6.91×10^{6}	7.72×10^{7}	2.13×10^{-8}
O_4	1.39×10^{-5}	99.9	7.97×10^{7}	8.82×10^{8}	1.86×10^{-9}
O_7	1.92×10^{-5}	97.8	2.77×10^{7}	6.51×10^{8}	2.64×10^{-9}
O_8	1.59×10^{-6}	95.8	2.21×10^{8}	7.79×10^{9}	2.23×10^{-10}
O_{11}	1.41×10^{-5}	97.5	4.58×10^{7}	8.74×10^{8}	1.95×10^{-9}
O_{12}	3.14×10^{-6}	95.4	1.16×10^{8}	3.93×10^{9}	4.42×10^{-10}
O_{13}	2.66×10^{-5}	96.9	1.24×10^{7}	4.73×10^{8}	3.69×10^{-9}
O_{14}	1.98×10^{-5}	96.9	1.48×10^{7}	6.38×10^{8}	2.74×10^{-9}

Table A.04: *Three-element Windkessel model parameters for FTA model.*

Output	$\bar{Q}$ [m^3/s]	$\bar{P}$ [mmHg]	R_1 [kg/m^4s]	R_2 [kg/m^4s]	C [m^4s^2/kg]
O_1	3.38×10^{-5}	105.4	2.20×10^{7}	3.93×10^{8}	4.31×10^{-9}
O_2	1.64×10^{-5}	98.9	5.00×10^{7}	7.52×10^{8}	2.23×10^{-9}
O_3	2.10×10^{-5}	98.9	3.91×10^{7}	5.90×10^{8}	2.85×10^{-9}
O_6	7.42×10^{-6}	99.9	8.56×10^{7}	1.71×10^{9}	9.97×10^{-10}
O_7	7.88×10^{-5}	97.8	7.66×10^{6}	1.58×10^{8}	1.08×10^{-8}
O_8	4.10×10^{-7}	95.8	1.49×10^{7}	3.11×10^{10}	5.75×10^{-11}
O_{11}	1.41×10^{-5}	97.5	5.26×10^{7}	8.70×10^{8}	1.94×10^{-9}
O_{12}	1.07×10^{-5}	95.4	5.10×10^{7}	1.14×10^{9}	1.51×10^{-9}
O_{13}	2.19×10^{-5}	96.9	1.86×10^{7}	5.72×10^{8}	3.03×10^{-9}
O_{14}	4.41×10^{-5}	96.9	8.50×10^{6}	2.84×10^{8}	6.12×10^{-9}
O_{16}	6.12×10^{-6}	96.9	1.49×10^{7}	2.09×10^{9}	8.48×10^{-10}

Table A.05: *Three-element Windkessel model parameters for IA model.*

Output	$\bar{Q}$ [m^3/s]	$\bar{P}$ [mmHg]	R_1 [kg/m^4s]	R_2 [kg/m^4s]	C [m^4s^2/kg]
O_1	2.78×10^{-5}	105.4	1.91×10^{7}	4.87×10^{8}	3.54×10^{-9}
O_2	2.80×10^{-5}	98.9	1.90×10^{7}	4.52×10^{8}	3.80×10^{-9}
O_3	2.77×10^{-5}	98.9	1.91×10^{7}	4.87×10^{8}	3.54×10^{-9}
O_7	7.65×10^{-6}	97.8	4.86×10^{7}	1.66×10^{9}	1.05×10^{-9}
O_8	3.27×10^{-5}	95.8	4.79×10^{6}	3.81×10^{8}	4.59×10^{-9}
O_{11}	1.98×10^{-5}	97.5	1.90×10^{7}	6.38×10^{8}	2.72×10^{-9}
O_{12}	3.27×10^{-5}	95.4	9.79×10^{6}	3.79×10^{8}	4.60×10^{-9}
O_{13}	3.55×10^{-5}	96.9	6.87×10^{6}	3.57×10^{8}	4.91×10^{-9}
O_{14}	3.55×10^{-5}	96.9	6.87×10^{6}	3.57×10^{8}	4.91×10^{-9}

Appendix B

New PimpleFluid Solver with Robin BC

The new PIMPLE solver with Robin BC is reported.

It is published online at this link: https://github.com/solids4foam/solids4foam/commit/ca2055177b9360fc0a10e16340c9b2172e5bb112.

The added code is highlighted in red and blue:

```
#include "pimpleFluid.H"
#include "addToRunTimeSelectionTable.H"
#include "findRefCell.H"
#include "adjustPhi.H"
#include "CorrectPhi.H"
#include "fv.H"
#include "fvc.H"
#include "fvm.H"
#include "constrainHbyA.H"
#include "constrainPressure.H"

#include "volFields.H"
#include "EulerDdtScheme.H"
#include "backwardDdtScheme.H"
#include "elasticSlipWallVelocityFvPatchVectorField.H"
#include "elasticWallVelocityFvPatchVectorField.H"
#include "elasticWallPressureFvPatchScalarField.H"

    // * * * * * * * * * * * * * * * * * * * * //

namespace Foam
{
```

```
namespace fluidModels
{

// * * * * * * * * Static Data Members * * ** * * * * //

defineTypeNameAndDebug(pimpleFluid, 0);
addToRunTimeSelectionTable(fluidModel,
pimpleFluid, dictionary);

// * * * * * * * * * Private Members * * * * * * * * * //

void pimpleFluid::updateRobinFsiInterfaceFlux()
{
forAll(U().boundaryField(), patchI)
{
if
(
(
isA<elasticWallPressureFvPatchScalarField>
(
p().boundaryField()[patchI]
)
&& isA<elasticSlipWallVelocityFvPatchVectorField>
(
U().boundaryField()[patchI]
)
)
|| (
isA<elasticWallPressureFvPatchScalarField>
(
p().boundaryField()[patchI]
)
&& isA<elasticWallVelocityFvPatchVectorField>
(
U().boundaryField()[patchI]
)
)
)
{
Info<< "Mesh changed: updating
flux on Robin interface.";
#ifdef OPENFOAMESIORFOUNDATION
```

```
phi().boundaryFieldRef()[patchI] = 0;
#else
phi().boundaryField()[patchI] = 0;
#endif
}
}
}

void pimpleFluid::updateRobinFsiInterface()
{
forAll(p().boundaryField(), patchI)
{
if
(
(
isA<elasticWallPressureFvPatchScalarField>
(
p().boundaryField()[patchI]
)
&& isA<elasticSlipWallVelocityFvPatchVectorField>
(
U().boundaryField()[patchI]
)
)
|| (
isA<elasticWallPressureFvPatchScalarField>
(
p().boundaryField()[patchI]
)
&& isA<elasticWallVelocityFvPatchVectorField>
(
U().boundaryField()[patchI]
)
)
)
{
const word ddtScheme =
#ifdef OPENFOAMESIORFOUNDATION
word(mesh().ddtScheme("ddt(" + U().name() +')'));
#else
mesh().schemesDict().ddtScheme("ddt(" + U.name() +')');
#endif
```

```
if
(
ddtScheme
== fv::EulerDdtScheme<vector>::typeName
)
{
phi().boundaryFieldRef()[patchI] =
phi().oldTime().boundaryField()[patchI];

rAUf_.boundaryFieldRef()[patchI] =
runTime().deltaT().value();
}
else if
(
ddtScheme
== fv::backwardDdtScheme<vector>::typeName
)
{
if(runTime().timeIndex() == 1)
{
#ifdef OPENFOAMESIORFOUNDATION
phi().boundaryFieldRef()[patchI] =
phi().oldTime().boundaryField()[patchI];
rAUf_.boundaryFieldRef()[patchI] = runTime().deltaT().value();
#else
phi.boundaryField()[patchI] =
phi.oldTime().boundaryField()[patchI];
rAUf.boundaryField()[patchI] =
runTime().deltaT().value();
#endif

phi().oldTime().oldTime();
}
else
{
scalar deltaT = runTime().deltaT().value();
scalar deltaT0 = runTime().deltaT0().value();

scalar Cn = 1 + deltaT/(deltaT + deltaT0);
scalar Coo = deltaT*deltaT/(deltaT0*(deltaT + deltaT0));
scalar Co = Cn + Coo;

#ifdef OPENFOAMESIORFOUNDATION
```

```
phi().boundaryFieldRef()[patchI] =
(Co/Cn)*phi().oldTime().boundaryField()[patchI]
- (Coo/Cn)
*phi().oldTime().oldTime().boundaryField()[patchI];

rAUf_.boundaryFieldRef()[patchI] =
runTime().deltaT().value()/Cn;
#else
phi.boundaryField()[patchI] =
(Co/Cn)*phi.oldTime().boundaryField()[patchI]
- (Coo/Cn)
*phi.oldTime().oldTime().boundaryField()[patchI];

rAUf.boundaryField()[patchI] =
runTime().deltaT().value()/Cn;
#endif
}
}
}
}
}

void pimpleFluid::correctRobinFsiInterfaceFlux()
{
forAll(p().boundaryField(), patchI)
{
if
(
(
isA<elasticWallPressureFvPatchScalarField>
(
p().boundaryField()[patchI]
)
&& isA<elasticSlipWallVelocityFvPatchVectorField>
(
U().boundaryField()[patchI]
)
)
|| (
isA<elasticWallPressureFvPatchScalarField>
(
p().boundaryField()[patchI]
)
```

```
&& isA<elasticWallVelocityFvPatchVectorField>
(
U().boundaryField()[patchI]
)
)
)
{
const word ddtScheme =
#ifdef OPENFOAMESIORFOUNDATION
word(mesh().ddtScheme("ddt(" + U().name() +')'));
#else
mesh().schemesDict().ddtScheme("ddt(" + U.name() +')');
#endif

if
(
ddtScheme
== fv::EulerDdtScheme<vector>::typeName
)
{
phi().boundaryFieldRef()[patchI] =
phi().oldTime().boundaryField()[patchI]
- p().boundaryField()
[
patchI
].snGrad()*runTime().deltaT().value()
*mesh().magSf().boundaryField()
[
patchI
];
}
else if
(
ddtScheme
== fv::backwardDdtScheme<vector>::typeName
)
{
if(runTime().timeIndex() == 1)
{
phi().boundaryFieldRef()[patchI] =
phi().oldTime().boundaryField()[patchI];

rAUf_.boundaryFieldRef()[patchI] =
```

```
runTime().deltaT().value();

phi().oldTime().oldTime();
}
else
{
scalar deltaT = runTime().deltaT().value();
scalar deltaT0 = runTime().deltaT0().value();

scalar Cn = 1 + deltaT/(deltaT + deltaT0);
scalar Coo = deltaT*deltaT/(deltaT0*(deltaT + deltaT0));
scalar Co = Cn + Coo;

#ifdef OPENFOAMESIORFOUNDATION
phi().boundaryFieldRef()[patchI] =(Co/Cn)*phi().oldTime().boundaryField
()[patchI]
- (Coo/Cn)
*phi().oldTime().oldTime().boundaryField()[patchI];

rAUf_.boundaryFieldRef()[patchI] =
runTime().deltaT().value()/Cn;
#else
phi.boundaryField()[patchI] =
(Co/Cn)*phi.oldTime().boundaryField()[patchI]
- (Coo/Cn)
*phi.oldTime().oldTime().boundaryField()[patchI];

rAUf.boundaryField()[patchI] =
runTime().deltaT().value()/Cn;
#endif
}
}
}
}
}

// * * * * * * * Constructors  * * * * *  * * * * //

pimpleFluid::pimpleFluid
(
Time& runTime,
const word& region
```

```
)
:
fluidModel(typeName, runTime, region),
LTS_(fv::localEulerDdt::enabled(mesh())),
trDeltaT_(),
Uf_(),

rAU_
(
IOobject
(
"rAU",
runTime.timeName(),
mesh(),
IOobject::READ_IF_PRESENT,
IOobject::AUTO_WRITE
),
mesh(),
runTime.deltaT(),
zeroGradientFvPatchScalarField::typeName
),
rAUf_
(
IOobject
(
"rAUf",
runTime.timeName(),
mesh(),
IOobject::NO_READ,
IOobject::NO_WRITE
),
mesh(),
runTime.deltaT(),
calculatedFvPatchScalarField::typeName
),

pressureReference_(p(), pimple().dict()),
laminarTransport_(U(), phi()),
turbulence_
(
incompressible::momentumTransportModel::New
(
U(), phi(), laminarTransport_
```

```
)
),
rho_(laminarTransport_.lookup("rho")),
ddtU_(fvc::ddt(U())),
correctPhi_(pimple().dict().lookupOrDefault
("correctPhi", false)),
checkMeshCourantNo_
(
pimple().dict().lookupOrDefault("checkMeshCourantNo", false)
),
moveMeshOuterCorrectors_
(
pimple().dict().lookupOrDefault
("moveMeshOuterCorrectors", false)
),
cumulativeContErr_(0)
{
mesh().setFluxRequired(p().name());
turbulence_->validate();

if (mesh().dynamic())
{
Info<< "Constructing face velocity Uf\n" << endl;

Uf_ = new surfaceVectorField
(
IOobject
(
"Uf",
runTime.timeName(),
mesh(),
IOobject::READ_IF_PRESENT,
IOobject::AUTO_WRITE
),
fvc::interpolate(U())

);

}

if (LTS_)
{
Info<< "Using LTS" << endl;
```

```
trDeltaT_ = tmp<volScalarField>
(
new volScalarField
(
IOobject
(
fv::localEulerDdt::rDeltaTName,
runTime.timeName(),
mesh(),
IOobject::READ_IF_PRESENT,
IOobject::AUTO_WRITE
),
mesh(),
dimensionedScalar(dimless/dimTime, 1),
extrapolatedCalculatedFvPatchScalarField::typeName
)
);
}
else
{
const fvMesh& mesh = this->mesh();
const surfaceScalarField& phi = this->phi();
#include "CourantNo.H"
}


}
// * * * * Member Functions  * * * * * * * * * //

tmp<vectorField> pimpleFluid::patchViscousForce
(const label patchID) const
{
tmp<vectorField> tvF
(
new vectorField(mesh().boundary()[patchID].size(),

vector::zero)
);

tvF.ref() = rho_.value()
*(
mesh().boundary()[patchID].nf()
```

```
& (-turbulence_->devTau()().boundaryField()[patchID])
);

return tvF;
}

tmp<scalarField> pimpleFluid::
patchPressureForce(const label patchID) const
{
tmp<scalarField> tpF
(
new scalarField(mesh().boundary()[patchID].size(), 0)
);

tpF.ref() = rho_.value()*p().boundaryField()[patchID];

return tpF;
}


bool pimpleFluid::evolve()
{
Info<< "Evolving fluid model: " << this->type() << endl;

// Take references
const Time& runTime = fluidModel::runTime();
pressureReference& pressureReference = pressureReference_;
dynamicFvMesh& mesh = this->mesh();
pimpleControl& pimple = this->pimple();
volVectorField& U = this->U();
volScalarField& p = this->p();
surfaceScalarField& phi = this->phi();
autoPtr<surfaceVectorField>& Uf = Uf_;
scalar& cumulativeContErr = cumulativeContErr_;


const bool correctPhi = correctPhi_;
const bool checkMeshCourantNo = checkMeshCourantNo_;
const bool moveMeshOuterCorrectors=moveMeshOuterCorrectors_;

// --- Pressure-velocity PIMPLE corrector loop
while (pimple.loop())
{
```

```
if (pimple.firstPimpleIter() || moveMeshOuterCorrectors)
{
    // fvModels not added yet
    //fvModels.preUpdateMesh();

// Ideally we would not need a specific FSI mesh
//update function
// Hopefully we can remove the need for it soon
if (fluidModel::fsiMeshUpdate())
    {
// The FSI interface is in charge of calling mesh.update()
fluidModel::fsiMeshUpdateChanged();
    }
    else
    {
        mesh.update();
    }

    if (mesh.changing())
    {
        // MRF not added yet
        //MRF.update();

        if (correctPhi)
        {
            #include "correctPhi.foundation.H"
        }

// Update flux in FSI interface with Robin BC
updateRobinFsiInterfaceFlux();


        if (checkMeshCourantNo)
        {
            #include "meshCourantNo.H"
        }

    }
}

// fvModels not implemented yet
//fvModels.correct();
```

```
// UEqn.H

// Solve the Momentum equation

// MRF not implemented yet
//MRF.correctBoundaryVelocity(U);

tmp<fvVectorMatrix> tUEqn
(
fvm::ddt(U) + fvm::div(phi, U)
// + MRF.DDt(U)
+ turbulence_->divDevSigma(U)
// ==
//    fvModels.source(U)
);
fvVectorMatrix& UEqn = tUEqn.ref();

UEqn.relax();

// fvConstraints not implemented yet
//fvConstraints.constrain(UEqn);

if (pimple.momentumPredictor())
{
solve(UEqn == -fvc::grad(p));

// fvConstraints not implemented yet
//fvConstraints.constrain(U);
}

// --- Pressure corrector loop
while (pimple.correct())
{


volScalarField rAU(1.0/UEqn.A());
volVectorField HbyA(constrainHbyA(rAU*UEqn.H(), U, p));
surfaceScalarField phiHbyA
(
"phiHbyA",
fvc::flux(HbyA)

);
```

```
if (p.needReference())
{
fvc::makeRelative(phiHbyA, U);
adjustPhi(phiHbyA, U, p);
fvc::makeAbsolute(phiHbyA, U);
}

tmp<volScalarField> rAtU(rAU);

if (pimple.consistent())
{
rAtU = 1.0/max(1.0/rAU - UEqn.H1(), 0.1/rAU);
phiHbyA +=
fvc::interpolate(rAtU()
- rAU)*fvc::snGrad(p)*mesh.magSf();
HbyA -= (rAU - rAtU())*fvc::grad(p);
}

if (pimple.nCorrPiso() <= 1)
{
tUEqn.clear();
}

// Update the pressure BCs to ensure flux consistency
// constrainPressure(p, U, phiHbyA, rAtU(), MRF);
constrainPressure(p, U, phiHbyA, rAtU());

// Update flux on the FSI interface for Robin BCs
updateRobinFsiInterface();

// Non-orthogonal pressure corrector loop
while (pimple.correctNonOrthogonal())
{
fvScalarMatrix pEqn
(
fvm::laplacian(rAtU(), p) == fvc::div(phiHbyA)
);

 pEqn.setReference
(
```

```
pressureReference.refCell(),
pressureReference.refValue()
);

pEqn.solve();

if (pimple.finalNonOrthogonalIter())
{
phi = phiHbyA - pEqn.flux();
}
}

#include "continuityErrs.H"
fluidModel::continuityErrs();


// Correct flux due for Robin BCs according
//to temporal discretization
correctRobinFsiInterfaceFlux();


// Explicitly relax pressure for momentum corrector
p.relax();

U = HbyA - rAtU*fvc::grad(p);
U.correctBoundaryConditions();
//fvConstraints.constrain(U);

// Correct Uf if the mesh is moving
fvc::correctUf(Uf, U, phi);

// Make the fluxes relative to the mesh motion
fvc::makeRelative(phi, U);



gradU() = fvc::grad(U);
ddtU_ = fvc::ddt(U);


// Make the fluxes absolute to the mesh motion
fvc::makeAbsolute(phi, U);
```

```
// Update velocity on faces to account for modifications in the flux
//when using the Robin BCs
Uf_() = fvc::interpolate(U, "interpolate(U)");

// Get tangential velocity
Uf_() -= (mesh.Sf() & Uf_())*mesh.Sf()/magSqr(mesh.Sf());

// Update with normal from flux
Uf_() += phi*mesh.Sf()/magSqr(mesh.Sf());


}

if (pimple.turbCorr())
{
laminarTransport_.correct();
turbulence_->correct();
}



}

return 0;
}


// * * * * * * * * * * * * * * * * * //

} // End namespace fluidModels
} // End namespace Foam

// ************************************************* //
```

List of Figures

List of Tables

Publications

Research Publications:

1. Moretti, S., Tauro, F., Orrico, M., Mangialardi, N., and Facci, A. L. Comparative Analysis of Patient-Specific Aortic Dissections through Computational Fluid Dynamics Suggests Increased Likelihood of Degeneration in Partially Thrombosed False Lumen. Bioengineering.(2023), 10(3), 316. https://doi.org/10.3390/ bioengineering10030316;

2. Being published: Moretti, S., Tauro, F., Facci, A. L. "FSI Simulation of Healty Aorta Model".

Other works:

1. Rontos, K., Mosconi, E.M., Gianvincenzi, M., Moretti, S., Salvati, L. Toward a Spatially Segregated Urban Growth? Austerity, Poverty, and the Demographic Decline of Metropolitan Greece. Data (2023), 8, 53. https://doi.org/ 10.3390/data8030053;

2. Meshkini A., and Ahmadifard N., Salvati L., Clemente M., Moretti S., Shahraki S.Z., Parikhane S. E., Pedestrians' Perception of Landscape Quality and Urban Liveability: A Field Survey in a Local Community of Tehran, Iran. International Journal of Statistics and Economics (2020), 21;

Bibliography

[1] World Health Organization, Cardiovascular diseases (CVDs) (2021). [link].
URL https://www.who.int/news-room/fact-sheets/detail/cardiovascular-diseases-(cvds)

[2] D. Mozaffarian, E. J. Benjamin, A. S. Go, D. K. Arnett, M. J. Blaha, M. Cushman, S. R. Das, S. de Ferranti, J.-P. DesprÃ©s, H. J. Fullerton, V. J. Howard, M. D. Huffman, C. R. Isasi, M. C. JimÃ©nez, S. E. Judd, B. M. Kissela, J. H. Lichtman, L. D. Lisabeth, S. Liu, R. H. Mackey, D. J. Magid, D. K. McGuire, E. R. Mohler, C. S. Moy, P. Muntner, M. E. Mussolino, K. Nasir, R. W. Neumar, G. Nichol, L. Palaniappan, D. K. Pandey, M. J. Reeves, C. J. Rodriguez, W. Rosamond, P. D. Sorlie, J. Stein, A. Towfighi, T. N. Turan, S. S. Virani, D. Woo, R. W. Yeh, M. B. Turner, Heart disease and stroke statistics-2016 update a report from the american heart association, Circulation 133 (4) (2016) e38–e48. doi:10.1161/CIR.0000000000000350.

[3] J. Soppert, M. Lehrke, N. Marx, J. Jankowski, H. Noels, Lipoproteins and lipids in cardiovascular disease: from mechanistic insights to therapeutic targeting, Advanced Drug Delivery Reviews 159 (2020) 4–33. doi:10.1016/j.addr.2020.07.019.

[4] D. Zhou, B. Xi, M. Zhao, L. Wang, S. P. Veeranki, Uncontrolled hypertension increases risk of all-cause and cardiovascular disease mortality in US adults: The NHANES III linked mortality study, Scientific Reports 8 (1) (2018) 1–7. doi:10.1038/s41598-018-27377-2.

[5] P. G. Hagan, C. A. Nienaber, E. M. Isselbacher, D. Bruckman, D. J. Karavite, P. L. Russman, A. Evangelista, R. Fattori, T. Suzuki,

J. K. Oh, et al., The international registry of acute aortic dissection (IRAD): new insights into an old disease, Jama 283 (7) (2000) 897–903. doi:10.1001/jama.283.7.897.

[6] W. C. Roberts, Aortic dissection: anatomy, consequences, and causes, American Heart Journal 101 (2) (1981) 195–214. doi:10.1016/0002-8703(81)90666-9.

[7] A. Tsamis, J. T. Krawiec, D. A. Vorp, Elastin and collagen fibre microstructure of the human aorta in ageing and disease: a review, Journal of the Royal Society Interface 10 (83). doi:10.1098/rsif.2012.1004.

[8] J. Golledge, K. A. Eagle, Acute aortic dissection, The Lancet 372 (9632) (2008) 55–66. doi:10.1016/S0140-6736(08)60994-0.

[9] M. Landenhed, G. Engström, A. Gottsäter, M. P. Caulfield, B. Hedblad, C. Newton-Cheh, O. Melander, J. G. Smith, Risk profiles for aortic dissection and ruptured or surgically treated aneurysms: a prospective cohort study, Journal of the American Heart Association 4 (1) (2015) e001513. doi:10.1161/JAHA.114.001513.

[10] H. Yin, J. G. Pickering, Cellular senescence and vascular disease: novel routes to better understanding and therapy, Canadian Journal of Cardiology 32 (5) (2016) 612–623. doi:10.1016/j.cjca.2016.02.051.

[11] J. Gawinecka, F. Schönrath, A. von Eckardstein, Acute aortic dissection: pathogenesis, risk factors and diagnosis, Swiss medical weekly 147 (2017) w14489. doi:10.4414/smw.2017.14489.

[12] D. P. Howard, A. Banerjee, J. F. Fairhead, J. Perkins, L. E. Silver, P. M. Rothwell, Population-based study of incidence and outcome of acute aortic dissection and premorbid risk factor control: 10-year results from the oxford vascular study, Circulation 127 (20) (2013) 2031–2037. doi:10.1161/CIRCULATIONAHA.112.000483.

[13] D. Juang, A. C. Braverman, K. Eagle, Aortic dissection, Circulation 118 (14) (2008) 507–510. doi:10.1161/CIRCULATIONAHA.108.799908.

[14] M. Koga, Y. Iguchi, T. Ohara, Y. Tahara, T. Fukuda, T. Noguchi, H. Matsuda, K. Minatoya, K. Nagatsuka, K. Toyoda, Acute ischemic stroke as a complication of Stanford type A acute aortic dissection: a review and proposed clinical recommendations for urgent diagnosis, General Thoracic and Cardiovascular Surgery 66 (8) (2018) 439–445. doi:10.1007/s11748-018-0956-4.

[15] C. A. Nienaber, R. E. Clough, N. Sakalihasan, T. Suzuki, R. Gibbs, F. Mussa, M. T. Jenkins, M. M. Thompson, A. Evangelista, J. S. Yeh, N. Cheshire, U. Rosendahl, J. Pepper, Aortic dissection, Nature Reviews Disease Primers 2 (July). doi:10.1038/nrdp.2016.53.

[16] S. Trimarchi, K. A. Eagle, C. A. Nienaber, V. Rampoldi, F. H. Jonker, C. De Vincentiis, A. Frigiola, L. Menicanti, T. Tsai, J. Froehlich, A. Evangelista, D. Montgomery, E. Bossone, J. V. Cooper, J. Li, M. G. Deeb, G. Meinhardt, T. M. Sundt, E. M. Isselbacher, Role of age in acute type A aortic dissection outcome: report from the international registry of Acute Aortic Dissection (IRAD), Journal of Thoracic and Cardiovascular Surgery 140 (4) (2010) 784–789. doi:10.1016/j.jtcvs.2009.11.014.

[17] D. Levy, A. Goyal, Y. Grigorova, F. Farci, J. K., Aortic Dissection (2021).
URL https://www.ncbi.nlm.nih.gov/books/NBK441963/

[18] V. Baliyan, A. Parakh, A. M. Prabhakar, S. Hedgire, Acute aortic syndromes and aortic emergencies, Cardiovascular Diagnosis and Therapy 8 (I) (2018) S82–S96. doi:10.21037/cdt.2018.03.02.

[19] W. D. Clouse, J. W. Hallett, H. V. Schaff, P. C. Spittell, C. M. Rowland, D. M. Ilstrup, L. J. Melton, Acute aortic dissection: population-based incidence compared with dgenerative aortic aneurysm rupture, Mayo Clinic Proceedings 79 (2) (2004) 176–180. doi:10.4065/79.2.176.

[20] X. Tang, K. Lu, X. Liu, D. Jin, W. Jiang, J. Wang, Y. Zhong, C. Wei, Y. Wang, P. Gao, J. Du, Incidence and survival of aortic dissection in urban China: results from the National Insurance Claims for Epidemiological Research (NICER) study, The Lancet Regional Health - Western Pacific 17 (2) (2021) 100280. doi:10.1016/j.lanwpc.2021.100280.

[21] L. F. Hiratzka, G. L. Bakris, J. A. Beckman, R. M. Bersin, V. F. Carr, D. E. Casey, K. A. Eagle, L. K. Hermann, E. M. Isselbacher, E. A. Kazerooni, N. T. Kouchoukos, B. W. Lytle, D. M. Milewicz, D. L. Reich, S. Sen, J. A. Shinn, L. G. Svensson, D. M. Williams, 2010 accf/ aha/ aats/ acr/ asa/ sca/ scai/ sir/ sts/ svm guidelines for the diagnosis and management of patients with thoracic aortic disease, Circulation 121 (13) (2010) e266–e369. doi:10.1161/CIR.0b013e3181d4739e.

[22] V. Aboyans, M. Boukhris, Dissecting the epidemiology of aortic dissection, European Heart Journal. Acute Cardiovascular Care 10 (7) (2021) 710–711. doi:10.1093/ehjacc/zuab065.

[23] U. K. Sampson, P. E. Norman, F. G. R. Fowkes, V. Aboyans, Y. Song, F. E. H. Jr., M. H. Forouzanfar, M. Naghavi, J. O. Denenberg, M. M. McDermott, M. H. Criqui, G. A. Mensah, M. Ezzati, C. Murray, Global and regional burden of aortic dissection and aneurysms: mortality trends in 21 world regions, 1990 to 2010, Global Heart 9 (1) (2014) 171–180.e10. doi:10.1016/j.gheart.2013.12.010.

[24] Y. C. Kumtap, C. Chundusu, V. Gomerep, S. Rapheal, r. P. Davwa, P. Dayom, I. Nwakwaka, Salam, D. SS., Ascending aortic dissection in the developing world; case report, Jos Journal of Medicine 12 (1) (2018) 1–6.

[25] R. Erbel, F. Alfonso, C. Boileau, O. Dirsch, B. Eber, A. Haverich, H. Rakowski, J. Struyven, K. Radegran, U. Sechtem, J. Taylor, C. Zollikofer, W. W. Klein, B. Mulder, L. A. Providencia, Diagnosis and management of aortic dissection: recommendations of the task force on aortic dissection, European Society of Cardiology, European Heart Journal 22 (18) (2001) 1642–1681. doi:10.1053/euhj.2001.2782.

[26] G. C. Hughes, Commentary: lack of screening makes primary prevention most effective to reduce the mortality of aortic dissection, Journal of Thoracic and Cardiovascular Surgery 161 (4) (2021) 1202–1203. doi:10.1016/j.jtcvs.2020.09.031.

[27] E. S. Crawford, L. G. Svensson, J. S. Coselli, H. J. Safi, K. R. Hess, Surgical treatment of aneurysm and/or dissection of the ascending

aorta, transverse aortic arch, and ascending aorta and transverse aortic arch. Factors influencing survival in 717 patients., The Journal of thoracic and cardiovascular surgery 98 (5 Pt 1) (1989) 654–659.

[28] M. E. DeBakey, C. H. McCollum, E. S. Crawford, G. C. J. Morris, J. Howell, G. P. Noon, G. Lawrie, Dissection and dissecting aneurysms of the aorta: twenty-year follow-up of five hundred twenty-seven patients treated surgically., Surgery 92 (6) (1982) 1118–1134.

[29] J. V. Lombardi, G. C. Hughes, J. J. Appoo, J. E. Bavaria, A. W. Beck, R. P. Cambria, K. Charlton-Ouw, M. H. Eslami, K. M. Kim, B. G. Leshnower, T. Maldonado, T. B. Reece, G. J. Wang, Society for Vascular Surgery (SVS) and Society of Thoracic Surgeons (STS) reporting standards for type B aortic dissections, Journal of Vascular Surgery 71 (3) (2020) 723–747. doi:https://doi.org/10.1016/j.jvs.2019.11.013.

[30] S. J. White, E. M. Hayes, S. Lehoux, J. Y. Jeremy, A. J. Horrevoets, A. C. Newby, Characterization of the differential response of endothelial cells exposed to normal and elevated laminar shear stress, Journal of Cellular Physiology 226 (11) (2011) 2841–2848. doi:10.1002/jcp.22629.

[31] R. PerinajovÃ¡, J. F. Juffermans, J. J. Westenberg, R. L. van der Palen, P. J. van den Boogaard, H. J. Lamb, S. KenjereÅ¡, Geometrically induced wall shear stress variability in cfd-mri coupled simulations of blood flow in the thoracic aortas, Computers in Biology and Medicine 133 (2021) 104385. doi:https://doi.org/10.1016/j.compbiomed.2021.104385.

[32] Z. Cheng, F. P. Tan, C. V. Riga, C. D. Bicknell, M. S. Hamady, R. G. Gibbs, N. B. Wood, X. Y. Xu, Analysis of flow patterns in a patient-specific aortic dissection model, Journal of Biomechanical Engineering 132 (5) (2010) 1–9. doi:10.1115/1.4000964.

[33] M. Chong, G. Boram, H. Armour, S. Dokos, Z. Ong, X. Xu, E. Lim, An integrated fluidâstructure interaction and thrombosis model for type b aortic dissection, Biomechanics and Modeling in Mechanobiologydoi:https://doi.org/10.1007/s10237-021-01534-55.

URL https://www.sciencedirect.com/science/article/pii/S000992602200736X

[34] A. Osswald, C. Karmonik, J. Anderson, F. Rengier, M. Karck, J. Engelke, K. Kallenbach, D. Kotelis, S. Partovi, D. BÃ¶ckler, A. Ruhparwar, Elevated Wall Shear Stress in aortic type B dissection may relate to retrograde aortic type A dissection: a computational fluid dynamics pilot study, European Journal of Vascular and Endovascular Surgery 54 (3) (2017) 324–330. doi:10.1016/j.ejvs.2017.06.012.

[35] Z. Cheng, N. B. Wood, R. G. Gibbs, X. Y. Xu, Geometric and flow features of type B aortic dissection: initial findings and comparison of medically treated and stented cases, Annals of Biomedical Engineering 43 (1) (2015) 177–189. doi:10.1007/s10439-014-1075-8.

[36] Z. Sun, T. Chaichana, A systematic review of computational fluid dynamics in type B aortic dissection, International Journal of Cardiology 210 (2016) 28–31. doi:10.1016/j.ijcard.2016.02.099.

[37] N. T. Philip, B. Patnaik, B. Sudhir, Hemodynamic simulation of Abdominal Aortic Aneurysm on idealised models : investigation of stress parameters during disease progression, Computer Methods and Programs in Biomedicine (2021) 106508doi:10.1016/j.cmpb.2021.106508.

[38] M. Varshney, M. Haani Farooqi, A. Y. Usmani, Quantifying hemodynamics within an aneurysm exposed to prolonged exercise levels, Computer Methods and Programs in Biomedicine 184 (2020) 105124. doi:https://doi.org/10.1016/j.cmpb.2019.105124.

[39] A. D. Caballero, S. Laín, A Review on computational fluid dynamics modelling in human thoracic aorta, Cardiovascular Engineering and Technology 4 (2) (2013) 103–130. doi:10.1007/s13239-013-0146-6.

[40] P. D. Morris, A. Narracott, H. von Tengg-Kobligk, D. A. Silva Soto, S. Hsiao, A. Lungu, P. Evans, N. W. Bressloff, P. V. Lawford, D. R. Hose, J. P. Gunn, Computational fluid dynamics modelling in cardiovascular medicine, Heart 102 (1) (2016) 18–28. doi:10.1136/heartjnl-2015-308044.

[41] R. Romarowski, M. Conti, S. Morganti, V. Grassi, M. Marrocco-Trischitta, S. Trimarchi, F. Auricchio, Computational simulation of tevar in the ascending aorta for optimal endograft selection: A patient-specific case study, Computers in Biology and Medicine 103 (2018) 140–147. doi:https://doi.org/10.1016/j.compbiomed.2018.10.014.

[42] S. Qin, B. Wu, J. Liu, W.-S. Shiu, Z. Yan, R. Chen, X.-C. Cai, Efficient parallel simulation of hemodynamics in patient-specific abdominal aorta with aneurysm, Computers in Biology and Medicine 136 (2021) 104652. doi:https://doi.org/10.1016/j.compbiomed.2021.104652.

[43] N. B. Langer, M. Argenziano, Minimally invasive cardiovascular surgery: incisions and approaches, Methodist DeBakey cardiovascular journal 12 (1) (2016) 4–9. doi:10.14797/mdcj-12-1-4.

[44] F. Gao, M. Watanabe, T. Matsuzawa, Stress analysis in a layered aortic arch model under pulsatile blood flow, BioMedical Engineering Online 5 (2006) 1–11. doi:10.1186/1475-925X-5-25.

[45] Z. Cheng, C. Riga, J. Chan, M. Hamady, N. B. Wood, N. J. Cheshire, Y. Xu, R. G. Gibbs, Initial findings and potential applicability of computational simulation of the aorta in acute type B dissection, Journal of Vascular Surgery 57 (2 SUPPL.) (2013) 35S–43S. doi:10.1016/j.jvs.2012.07.061.

[46] Y. Zhu, X. Xu, U. Rosendahl, J. Pepper, S. Mirsadraee, Advanced risk prediction for aortic dissection patients using imaging-based computational flow analysis, Clinical Radiologydoi:https://doi.org/10.1016/j.crad.2022.12.001.
URL https://www.sciencedirect.com/science/article/pii/S000992602200736X

[47] G. Biglino, D. Cosentino, J. A. Steeden, L. De Nova, M. Castelli, H. Ntsinjana, G. Pennati, A. M. Taylor, S. Schievano, Using 4D cardiovascular magnetic resonance imaging to validate computational fluid dynamics: a case study, Frontiers in Pediatrics 3Th (December) (2015) 1–10. doi:10.3389/fped.2015.00107.

[48] Z. Cheng, C. Juli, N. B. Wood, R. G. Gibbs, X. Y. Xu, Predicting flow in aortic dissection: comparison of computational model with PC-MRI velocity measurements, Medical Engineering and Physics 36 (9) (2014) 1176–1184. doi:10.1016/j.medengphy.2014.07.006.

[49] D. Dillon-Murphy, A. Noorani, D. Nordsletten, C. A. Figueroa, Multi-modality image-based computational analysis of haemodynamics in aortic dissection, Biomechanics and Modeling in Mechanobiology 15 (4) (2016) 857–876. doi:10.1007/s10237-015-0729-2.

[50] A. Leuprecht, S. Kozerke, P. Boesiger, K. Perktold, Blood flow in the human ascending aorta: a combined MRI and CFD study, Journal of Engineering Mathematics 47 (3-4) (2003) 387–404. doi:10.1023/B:ENGI.0000007969.18105.b7.

[51] Y. Zhu, R. Chen, Y. H. Juan, H. Li, J. Wang, Z. Yu, H. Liu, Clinical validation and assessment of aortic hemodynamics using computational fluid dynamics simulations from computed tomography angiography, BioMedical Engineering Online 17 (1) (2018) 1–12. doi:10.1186/s12938-018-0485-5.

[52] M. Bonfanti, S. Balabani, J. P. Greenwood, S. Puppala, S. Homer-Vanniasinkam, V. Diáz-Zuccarini, Computational tools for clinical support: a multi-scale compliant model for haemodynamic simulations in an aortic dissection based on multi-modal imaging data, Journal of the Royal Society Interface 14 (136). doi:10.1098/rsif.2017.0632.

[53] Q. Wang, X. Guo, E. K. W. Poon, A. Ooi, R. P. Lim, Three-dimensional CFD simulation of blood flow in aortic dissection, in: Proceedings of the 22nd Australasian Fluid Mechanics Conference AFMC2020, The University of Queensland, Brisbane, QLD Australia, 2020, pp. 7–10. doi:10.14264/5d0bea7.

[54] Y. Hohri, S. Numata, K. Itatani, K. Kanda, S. Yamazaki, T. Inoue, H. Yaku, Prediction for future occurrence of type A aortic dissection using computational fluid dynamics, European Journal of Cardio-thoracic Surgery 60 (2) (2021) 384–391. doi:10.1093/ejcts/ezab094.

[55] C. Karmonik, J. X. Bismuth, M. G. Davies, A. B. Lumsden, Computational hemodynamics in the human aorta : A computational fluid dynamics study of three cases with patient-specific geometries and inflow rates, Technology and health care : official journal of the European Society for Engineering and Medicine 16 (2008) 343–354.

[56] T. Canchi, S. D. Kumar, E. Y. Ng, S. Narayanan, A review of computational methods to predict the risk of rupture of abdominal aortic aneurysms, BioMed Research International 2015. doi:10.1155/2015/861627.

[57] M. Alimohammadi, J. M. Sherwood, M. Karimpour, A. Obiekezie, S. Balabani, V. DÃaz-Zuccarini, Aortic dissection simulation models for clinical support: fluid-structure interaction vs. rigid wall models, BioMedical Engineering OnLine 14. doi:https://doi.org/10.1186/s12938-015-0032-6.

[58] A. G. Brown, Y. Shi, A. Marzo, C. Staicu, I. Valverde, F. Beerbaum, P. V. Lawford, D. R. Hose, Accuracy vs. computational time: translating aortic simulations to the clinic., BioMedical Engineering OnLine 45. doi:https://10.1016/j.jbiomech.2011.11.041.

[59] D. C. Iliopoulos, E. P. Kritharis, A. T. Giagini, S. A. Papadodima, D. P. Sokolis, Ascending thoracic aortic aneurysms are associated with compositional remodeling and vessel stiffening but not weakening in age-matched subjects, The Journal of Thoracic and Cardiovascular Surgery 137 (1) (2009) 101–109. doi:https://doi.org/10.1016/j.jtcvs.2008.07.023.
URL https://www.sciencedirect.com/science/article/pii/S0022522308012026

[60] E. Vignali, E. Gasparotti, S. Celi, S. Avril, Fully-coupled fsi computational analyses in the ascending thoracic aorta using patient-specific conditions and anisotropic material properties, Frontiers in Physiology 12. doi:10.3389/fphys.2021.732561.

[61] S. Sherifova, G. A. Holzapfel, Biomechanics of aortic wall failure with a focus on dissection and aneurysm: A review., Acta Biomaterialiadoi:10.1016/j.actbio.2019.08.017.

[62] K. Khanafer, R. Berguer, Fluid-structure interaction analysis of turbulent pulsatile flow within a layered aortic wall as related to aortic dissection., Journal of biomechanics 42. doi:10.1016/j.jbiomech.2009.08.010.

[63] T. Zeljko, A. Karaĉ, P. Cardiff, H. Jasak, A. Ivanković., Openfoam finite volume solver for fluid-solid interaction.doi:https://doi.org/10.21278/TOF.42301.

[64] Z. Tukovic, A. Horvat, L. Virag, P. Milovic, I. BatistiÄ, Added-mass partitioned fluid-structure interaction solver for aorta dissection blood flow, 2022.

[65] Z. Tukovic, M. BukaÄ, P. Cardiff, H. Jasak, A. Ivankovic, Added Mass Partitioned FluidâStructure Interaction Solver Based on a Robin Boundary Condition for Pressure, 2018. doi:10.1007/978-3-319-60846-4_1.

[66] T. J. Pedley, The Fluid Mechanics of Large Blood Vessels, Cambridge University Press, Cambridge, 1980. doi:10.1017/cbo9780511896996.

[67] K. M. Tse, P. Chiu, H. P. Lee, P. Ho, Investigation of hemodynamics in the development of dissecting aneurysm within patient-specific dissecting aneurismal aortas using computational fluid dynamics (CFD) simulations, Journal of Biomechanics 44 (5) (2011) 827–836. doi:10.1016/j.jbiomech.2010.12.014.

[68] K. Perktold, R. Peter, Numerical 3D-simulation of pulsatile wall shear stress in an arterial T-bifurcation model, Journal of Biomedical Engineering 12 (1) (1990) 2–12. doi:10.1016/0141-5425(90)90107-X.

[69] V. KoláÅ, Vortex identification: new requirements and limitations, International Journal of Heat and Fluid Flow 28 (4) (2007) 638–652. doi:10.1016/j.ijheatfluidflow.2007.03.004.

[70] OpenFoam, User Guide-CFD Direct.
URL https://cfd.direct/openfoam/user-guide/v6-fvsolution/

[71] O. S. Pianykh, Springer Berlin Heidelberg, 2012. doi:10.1007/978-3-642-10850-1.

[72] R. C. Gonzalez, R. E. Woods, S. L. Eddins, Digital image processing using MATLAB, Pearson Prentice-Hall, Upper Saddle River, 2004.

[73] R. Mcneel, Rhinoceros 5 user ' s guide table of contents section I : introduction (2014).
URL http://docs.mcneel.com/rhino/5/usersguide/en-us/index.htm

[74] Mesh2surface, Mesh2Surface help.
URL http://www.mesh2surface.com/?p=samples

[75] C. C. Kai, G. G. Jacob, T. Mei, Interface between CAD and rapid prototyping systems. Part 1: A study of existing interfaces, International Journal of Advanced Manufacturing Technology 13 (8) (1997) 566–570. doi:10.1007/BF01176300.

[76] J. Lantz, R. Gårdhagen, M. Karlsson, Quantifying turbulent wall shear stress in a subject specific human aorta using large eddy simulation, Medical Engineering and Physics 34 (8) (2012) 1139–1148. doi:10.1016/j.medengphy.2011.12.002.

[77] M. Ferziger, Perić, R. L. Street, Computational methods for fluid dynamics, Vol. 3, Springer, Argovia, 2002.

[78] D. Wilcox, Turbulence modeling for CFD, DCW Industries, Inc, La Canada, 1993.

[79] B. E. Launder, B. I. Sharma, Application of the energy-dissipation model of turbulence to the calculation of flow near a spinning disc, Letters in Heat and Mass Transfer 1 (2) (1974) 131–137. doi:10.1016/0094-4548(74)90150-7.

[80] A. Hedlund, Evaluation of RANS turbulence models for the simulation of channel flow, Tech. rep. (2014).
URL http://urn.kb.se/resolve?urn=urn:nbn:se:uu:diva-238649

[81] H. Abreu, L. Eça, G. Saraiva, G. Vaz, Pros and Cons of Wall Functions, in: ASME 2015 34th International Conference on Ocean, Off-

shore and Arctic Engineering, St. John's, Newfoundland, Canada, 2018.

[82] H. Jasak, H. G. Weller, A. D. Gosman, High resolution NVD differencing scheme for arbitrarily unstructured meshes, International Journal for Numerical Methods in Fluids 31 (2) (1999) 431–449. doi:10.1002/(SICI)1097-0363(19990930)31:2<431::AID-FLD884>3.0.CO;2-T.

[83] The OpenFOAM Foundation, OpenFoam (2019).
URL https://openfoam.org/

[84] R. Issa, Solution of the implicitly discretised fluid flow equations by operator-splitting, Journal of Computational Physics 62 (1986) 40–65. doi:10.1016/0021-9991(86)90099-9.

[85] ESI-OpenCFD, The toolbox CFD open source, User Guide.
URL https://www.openfoam.com/

[86] M. Frigo, S. Johnson, FFTW: an adaptive software architecture for the FFT., in: Proceedings of the International Conference on Acoustics, Speech, and Signal Processing., Vol. 3, 1998, pp. 1381–1384. doi:10.1109/ICASSP.1998.681704.

[87] A. Quarteroni, T. Lassila, S. Rossi, R. Ruiz-Baier, Integrated heartâcoupling multiscale and multiphysics models for the simulation of the cardiac function, Computer Methods in Applied Mechanics and Engineering 314 (2017) 345–407. doi:https://doi.org/10.1016/j.cma.2016.05.031.

[88] M. Markl, M. T. Draney, M. D. Hope, J. M. Levin, F. P. Chan, M. T. Alley, N. J. Pelc, R. J. Herfkens, Time-resolved 3-dimensional velocity mapping in the thoracic aorta, Journal of Computer Assisted Tomography 28 (4) (2004) 459–468. doi:10.1097/00004728-200407000-00005.

[89] P. F. Fischer, F. Loth, S. E. Lee, S.-W. Lee, D. S. Smith, H. S. Bassiouny, Simulation of high-reynolds number vascular flows, Computer Methods in Applied Mechanics and Engineering 196 (31) (2007) 3049–3060, computational Bioengineering. doi:https://doi.org/10.1016/j.cma.2006.10.015.

[90] A. Quarteroni, A. Veneziani, C. Vergara, Geometric multiscale modeling of the cardiovascular system, between theory and practice, Computer Methods in Applied Mechanics and Engineering 302 (2016) 193–252. doi:10.1016/j.cma.2016.01.007.

[91] S. Pirola, Z. Cheng, O. A. Jarral, D. P. O'Regan, J. R. Pepper, T. Athanasiou, X. Y. Xu, On the choice of outlet boundary conditions for patient-specific analysis of aortic flow using computational fluid dynamics, Journal of Biomechanics 60 (2017) 15–21. doi:10.1016/j.jbiomech.2017.06.005.

[92] B. C. Systems, ANSA version 20.1.x User Guide (2019).

[93] Symscape, Polyhedral, Tetrahedral, and Hexahedral Mesh Comparison (2013).
URL https://www.symscape.com/

[94] A. L. Facci, R. Panciroli, S. Ubertini, M. Porfiri, Assessment of PIV-based analysis of water entry problems through synthetic numerical datasets, Journal of Fluids and Structures 55 (2015) 484–500. doi:10.1016/j.jfluidstructs.2015.03.018.

[95] D. S. Rawat, M. Pourquie, C. Poelma, Numerical investigation of turbulence in abdominal aortic aneurysms, Journal of Biomechanical Engineering 141 (6). doi:10.1115/1.4043289.

[96] J. Alastruey, K. Parker, S. Sherwin, Arterial pulse wave haemodynamics, Virtual PiE Led t/a BHR Group, 2012, pp. 401–442.

[97] N. Xiao, J. Alastruey, C. Alberto Figueroa, A systematic comparison between 1-D and 3-D hemodynamics in compliant arterial models, International Journal for Numerical Methods in Biomedical Engineering 30 (2) (2014) 204–231. doi:10.1002/cnm.2598.

[98] J. Yull Park, C. Young Park, C. Mo Hwang, K. Sun, B. Goo Min, Pseudo-organ boundary conditions applied to a computational fluid dynamics model of the human aorta, Computers in Biology and Medicine. 37 (8) (2007) 1063–1072. doi:10.1016/j.compbiomed.2006.09.012.

[99] B. Fitzgibbon, F. Jordan, N. Hynes, J. McGarry, E. P. Kavanagh, P. McHugh, D. Veerasingam, S. Sultan, Endovascular versus open

surgical repair for complicated chronic type b aortic dissection, The Cochrane Database of Systematic Reviews 2018 (4). doi:10.1002/14651858.CD012992.pub2.

[100] R. Zorrilla, E. Soudah, R. Rossi, Computational modeling of the fluid flow in type B aortic dissection using a modified finite element embedded formulation, Biomechanics and Modeling in Mechanobiology 19 (5) (2020) 1565–1583. doi:10.1007/s10237-020-01291-x.

[101] M. S. Zakaria, F. Ismail, M. Tamagawa, A. F. Abdul Azi, S. Wiriadidjaya, A. A. Basri, K. A. Ahmad, Computational fluid dynamics study of blood flow in aorta using OpenFOAM, Journal of Advanced Research in Fluid Mechanics and Thermal Sciences 43 (1) (2018) 81–89.

[102] A. Brandstädt, R. Mosca, On variations of P4-sparse graphs, Discrete Applied Mathematics 129 (2-3) (2003) 521–532. doi:10.1016/s0166-218x(03)00180-x.

[103] C. W. Ong, I. Wee, N. Syn, S. Ng, H. L. Leo, A. M. Richards, A. M. Choong, Computational fluid dynamics modeling of hemodynamic parameters in the human diseased aorta: a systematic review, Annals of Vascular Surgery 63 (2020) 336–381. doi:10.1016/j.avsg.2019.04.032.

[104] M. Gonzalez-Urquijo, R. G. de Zamacona, A. K. M. Mendoza, M. Z. Iribarren, E. G. Ibarra, M. D. M. Bencomo, M. A. Fabiani, 3d modeling of blood flow in simulated abdominal aortic aneurysm., Vascular and Endovascular Surgery 55.

[105] Q. Chi, Y. He, Y. Luan, K. Qin, L. Mu, Numerical analysis of wall shear stress in ascending aorta before tearing in type A aortic dissection, Computers in Biology and Medicine 89 (November 2016) (2017) 236–247. doi:10.1016/j.compbiomed.2017.07.029.

[106] A. Polanczyk, A. Piechota-Polanczyk, C. Neumayer, I. Huk, Cfd reconstruction of blood hemodynamic based on a self-made algorithm in patients with acute type iiib aortic dissection treated with tevar procedure, in: IUTAM Symposium on Recent Advances in Moving Boundary Problems in Mechanics, Springer International Publishing, Cham, 2019, pp. 75–84.

[107] D. A. Steinman, Image-based computational fluid dynamics modeling in realistic arterial geometries, Annals of Biomedical Engineering 30 (4) (2002) 483–497. doi:10.1114/1.1467679.

[108] A. Sequeira, J. Janela, An overview of some mathematical models of blood rheology, A Portrait of State-of-the-Art Research at the Technical University of Lisbon 29 (2007) 65–87. doi:https://doi.org/10.1002/cnm.2523.

[109] J. Febina, M. Y. Sikkandar, N. M. Sudharsan, Wall Shear Stress estimation of thoracic aortic aneurysm using computational fluid dynamics, Computational and Mathematical Methods in Medicine 2018. doi:10.1155/2018/7126532.

[110] F. Y., M. Y. G., A critical -review-on blood flow in large arteries., Korea-Australia Rheology Journal. 20 (4) (2008) 197–211.

[111] J. Xiang, M. Tremmel, J. Kolega, E. I. Levy, S. K. Natarajan, H. Meng, Newtonian viscosity model could overestimate wall shear stress in intracranial aneurysm domes and underestimate rupture risk., Journal of NeuroInterventional Surgery 20 (5) (2012) 351–357.

[112] M. A. H. Mohd Adib, L. Sheh Hong, M. S. Abdullah, R. Hassan, S. Wada, A perspective review: technical study of combining phase contrast magnetic resonance imaging and computational fluid dynamics for blood flow on carotid bifurcation artery, Journal of Mechanical Engineering and Sciences 14 (4) (2020) 7609–7621. doi:10.15282/jmes.14.4.2020.25.0599.

[113] P. Cardiff, A. KaraÄ, P. Jaeger, H. Jasak, J. Nagy, A. Ivankovic, Z. Tukovic, An open-source finite volume toolbox for solid mechanics and fluid-solid interaction simulations.

[114] S. T. Ha, L. C. Ngo, M. Saeed, B. J. Jeon, H. Choi, A comparative study between partitioned and monolithic methods for the problems with 3d fluid-structure interaction of blood vessels, Journal of Mechanical Science and Technology 31 (2017) 281–287.

[115] S. C. M. Christine M Scotti, Alexander D Shkolnik, E. A. Finol, Fluid-structure interaction in abdominal aortic aneurysms: effects of asymmetry and wall thickness, BioMedical Engineering OnLine 4 (2005) 64. doi:https://doi.org/10.1186/1475-925X-4-64.

[116] A. M. S. J. S. P. C. G. M. F. P. C. M. P. F. A. L. M. . D. F. Kathrin BÃ¤umler, Vijay Vedula, Fluidâstructure interaction simulations of patient-specific aortic dissection, Biomechanics and Modeling in Mechanobiology (21) (2020) 1607â1628. doi:https://doi.org/10.1007/s10237-020-01294-8.

[117] E. Gentleman, A. N. Lay, D. A. Dickerson, E. A. Nauman, G. A. Livesay, K. C. Dee, Mechanical characterization of collagen fibers and scaffolds for tissue engineering, Biomaterials 24 (21) (2003) 3805–3813. doi:https://doi.org/10.1016/S0142-9612(03)00206-0.
URL https://www.sciencedirect.com/science/article/pii/S0142961203002060

[118] N. T. Philip, B. Patnaik, B. Sudhir, Hemodynamic simulation of abdominal aortic aneurysm on idealised models: Investigation of stress parameters during disease progression, Computer Methods and Programs in Biomedicine 213 (2022) 106508. doi:https://doi.org/10.1016/j.cmpb.2021.106508.
URL https://www.sciencedirect.com/science/article/pii/S0169260721005824

[119] R. Torii, M. Oshima, T. Kobayashi, K. Takagi, T. E. Tezduyar, Fluidâstructure interaction modeling of a patient-specific cerebral aneurysm: influence of structural modeling, Computational Mechanics 43 (2008) 151–159. doi:https://doi.org/10.1007/s00466-008-0325-8.

[120] Y. Qiao, Y. Zeng, Y. Ding, J. Fan, K. Luo, T. Zhu, Numerical simulation of two-phase non-newtonian blood flow with fluid-structure interaction in aortic dissection, Computer Methods in Biomechanics and Biomedical Engineering 22 (6) (2019) 620–630. doi:10.1080/10255842.2019.1577398.

[121] G. Nannini, A. Caimi, M. C. Palumbo, S. Saitta, L. N. Girardi, M. Gaudino, M. J. Roman, J. W. Weinsaft, A. Redaelli, Aortic hemodynamics assessment prior and after valve sparing reconstruction: A patient-specific 4d flow-based fsi model, Computers in Biology and Medicine 135 (2021) 104581. doi:https://doi.org/10.1016/j.compbiomed.2021.104581.

[122] S. Kang, H. Choi, J. Yoo, Investigation of fluid structure interactions using a velocity linked p2/p1 finite element method and the generalized-α method, International Journal for Numerical Methods in Engineering 90 (12) (2012) 1529–1548. doi:https://doi.org/10.1002/nme.4252.

[123] R. Gnyaneshwar, R. K. Kumar, K. R. Balakrishnan, Dynamic analysis of the aortic valve using a finite element model, The Annals of Thoracic Surgery 73 (4) (2002) 1122–1129. doi:https://doi.org/10.1016/S0003-4975(01)03588-3.

[124] Cardiff, solids4foam.
URL https://solids4foam.github.io/

[125] OpenFoam, OpenFOAM v9 — Patch Releases.
URL https://openfoam.org/news/v9-patch/

[126] H. Jasak, Z. Tukovic, Automatic mesh motion for the unstructured finite volume method, Transactions of FAMENA 30 (2006) 1–20.

[127] C. Kassiotis, Which strategy to move the mesh in the computational fluid dynamic code openfoam, 2008.
URL https://perso.crans.org/kassiotis/openfoam/movingmesh.pdf

[128] A. Horvat, Ž. Tuković, Comparison between fluid-structure interaction simulations and computational fluid dynamics applied to thoracic aorta.

[129] P. Farrell, J. Maddison, Conservative interpolation between volume meshes by local galerkin projection, Computer Methods in Applied Mechanics and Engineering 200 (1) (2011) 89–100. doi:https://doi.org/10.1016/j.cma.2010.07.015.

[130] B. M. Irons, R. C. Tuck, A version of the aitken accelerator for computer iteration, International Journal for Numerical Methods in Engineering 1 (3) (1969) 275–277. doi:https://doi.org/10.1002/nme.1620010306.

[131] U. Küttler, W. A. Wall, Fixed-point fluid-structure interaction solvers with dynamic relaxation, Computational Mechanics 43. doi:https://doi.org/10.1007/s00466-008-0255-5.

[132] K. Bäumler, V. Vedula, A. M. Sailer, J. Seo, P. Chiu, G. Mistelbauer, F. P. Chan, M. P. Fischbein, A. L. Marsden, D. Fleischmann, Fluidâstructure interaction simulations of patient-specific aortic dissection, Biomechanics and Modeling in Mechanobiology 19 (5) (2020) 1607–1628. doi:10.1007/s10237-020-01294-8.

[133] P. Moireau, N. Xiao, M. Astorino, C. A. Figueroa, D. Chapelle, C. A. Taylor, J.-F. Gerbeau, External tissue support and fluidâstructure simulation in blood flows, Biomechanics and Modeling in Mechanobiology 11. doi:https://doi.org/10.1007/s10237-011-0289-z.

[134] F. Gao, T. Matsuzawa, Fsi within aortic arch model over cardiac cycle and influence of wall stiffness on wall stress in layered wall, Engineering Letters 13.

[135] S. Miyazaki, K. Itatani, T. Furusawa, T. Nishino, M. Sugiyama, Y. Takehara, S. Yasukochi, Validation of numerical simulation methods in aortic arch using 4d flow mri, Heart and Vessels 32. doi:https://doi.org/10.1007/s00380-017-0979-2.

[136] A. Qiao, W. Yin, B. Chu, Numerical simulation of fluidâstructure interaction in bypassed debakey iii aortic dissection, Computer Methods in Biomechanics and Biomedical Engineering 18 (11) (2015) 1173–1180. doi:10.1080/10255842.2014.881806.

[137] P. Reymond, P. Crosetto, S. Deparis, A. Quarteroni, N. Stergiopulos, Physiological simulation of blood flow in the aorta: Comparison of hemodynamic indices as predicted by 3-d fsi, 3-d rigid wall and 1-d models, Medical Engineering Physics 35 (6) (2013) 784–791. doi:https://doi.org/10.1016/j.medengphy.2012.08.009.
URL https://www.sciencedirect.com/science/article/pii/S1350453312002226

Ringraziamenti

Ringrazio tutti coloro che mi hanno supportato durante il percorso per raggiungere questo importante traguardo.

Vorrei ringraziare il Prof. Andrea L. Facci, il Prof. Danilo Monarca e la Prof. ssa Flavia Tauro per la loro preziosa guida e per la possibilità concessami di intraprendere questo bellissimo percorso.

Un ringraziamento sentito a tutti gli amici e colleghi dell'Unitus che con la loro presenza e il loro supporto hanno reso indimenticabili questi anni di formazione.